Numerical Simulation of the Meso-β Scale Structure and Evolution of the 1977 Johnstown Flood. Part I: Model Description and Verification

DA-LIN ZHANG AND J. MICHAEL FRITSCH

Department of Meteorology, The Pennsylvania State University, University Park, PA 16802

(Manuscript received 4 September 1985, in final form 10 March 1986)

ABSTRACT

The Pennsylvania State University/NCAR mesoscale model, originally developed by Anthes and Warner, is modified to simulate the meso-β scale structure and evolution of convectively driven weather systems. The modifications include: (i) two-way interactive nested-grid procedures, (ii) the Fritsch–Chappell convective parameterization scheme, and (iii) the Blackadar boundary layer package.

An 18-h simulation of the Johnstown flood of July 1977 is conducted. Compared to the documentation of Hoxit et al. and Bosart and Sanders, the simulation reproduced many of the different aspects of the mesoscale convective complex and squall line that were responsible for the heavy rain over western Pennsylvania. In particular, the model predicts the size, propagation rate and orientation of the mesoscale convective components that were observed in the mid-Atlantic states. The simulated evolution of the planetary boundary layer, cool outflow boundaries and surface pressure perturbations, such as meso-β scale lows, highs, ridges and troughs, compare favorably to observations. Other mesoscale features, for example, low-level jets and maximum/minimum horizontal wind couplets associated with the convective systems, were also reproduced reasonably well. Of particular significance is that the model-forecast rainfall amounts and distribution are similar to the observed.

Recognizing that a single case study does not provide a rigorous test of the predictability of a model, the results suggest that it may be possible to forecast the meso-β scale structure and evolution of convective weather systems with useful skill for periods up to about 18 hours. The results also suggest that significant improvements in warm-season quantitative precipitation forecasts might be possible if numerical forecasts of the meso-β scale structure and evolution of convective weather systems became operational.

1. Introduction

Although numerical predictions of large-scale circulation patterns have improved markedly during the past three decades, quantitative precipitation forecasts (QPFs) have proven to be a particularly stubborn problem to solve and progress has been slow. This is especially true for warm-season QPFs (Ramage, 1982; Georgakakos and Hudlow, 1984). Several studies (e.g., Charba and Klein, 1980; UCAR, 1983) attribute this problem to the fact that daily precipitation primarily occurs in mesoscale time and space, and that a large portion of the precipitation is associated with mesoscale convective systems (MCSs) in which thermodynamic structure dominates dynamic processes. If this is true, then it may be possible to improve the warm-season QPFs through successful predictions of the meso-β scale structure and evolution of MCSs. It is hypothesized that such predictions critically depend on initial conditions, lateral boundary conditions, model resolution, and particularly the inclusion of diabatic heating, planetary boundary layer (PBL) processes and terrain effects. This paper is the first in a series of papers that examine this hypothesis using an 18-h numerical simulation of the Johnstown, Pennsylvania, flash flood of 19–20 July 1977 (hereafter referred to as the Johnstown flood). The reasons for choosing the Johnstown flood are as follows:

First, observational studies by Hoxit et al. (1978) and Bosart and Sanders (1981), hereafter referred to as H78 and BS81, respectively, documented the occurrence of a number of meteorological phenomena which would provide a multifaceted and rigorous test of the hypothesis. Specifically, during the period encompassing the flood, the model would have to "predict" (i) the evolution of a traveling short wave; (ii) development and evolution of a squall line and mesoscale convective complex (MCC, see Maddox, 1980 for definition); (iii) the nocturnal behavior of the MCSs; (iv) separation of the squall line and the MCC convective systems; (v) development of meso-β scale surface highs, lows and cool outflow boundaries; (vi) generation of a mesoscale warm-core vortex; (vii) heavy precipitation at preferred locations; (viii) mesoscale terrain forcing; (ix) the diurnal cycle of the planetary boundary layer; (x) maintenance of a low-level jet; and (xi) propagation of internal gravity waves accompanying the MCSs. All these meso-β to meso-α scale features provide, in a single case, a particularly severe and challenging test for the above hypothesis. Moreover, up to now, there are no numerical models being run

with real data that are capable of predicting meso-β scale structures, such as mesohighs, mesolows, mesovortices and outflow boundaries. These meso-β scale aspects have been found to be very important for the development and organization of the MCSs in the Johnstown flood (H78) and other cases (Maddox et al., 1979; McAnelly and Cotton, 1981).

Second, the Johnstown flood constituted a major meteorological disaster in recent history. Yet the operational Limited-Area Fine-Mesh Model (LFM) forecasts failed to predict any precipitation across the northeastern United States during the 24-h period encompassing the flood and were especially deficient in preserving the upper-level short wave associated with the migratory MCS. For both the operational and research communities, this case has attracted much attention and concern with respect to the improvement of model-output guidance, severe weather warnings and the warm-season QPF. In addition to the diagnostic studies mentioned before, several numerical studies have also been conducted (Kreitzberg and Perkey, personal communication, 1983; Molinari and Corsetti, 1985). Results of Molinari and Corsetti's study primarily focused on the prediction of total precipitation and the meso-β scale structures apparently were not considered.

Third, the Johnstown flood case has been well documented by H78 and BS81. Thus, strict and careful comparisons between the simulations and the observations are possible, and this greatly facilitates understanding of the problems related to prediction of MCSs and the warm-season QPF. In particular, in conducting their diagnostic studies, BS81 subjectively generated a mesoscale dataset for 1200 GMT 19 July and 0000 GMT 20 July 1977 for the eastern United States. This valuable dataset fills gaps in the poor density of standard initial sounding data and provides a good basis for the numerical case study.

The objectives of this paper are to 1) document the modifications and improvements that were incorporated into The Pennsylvania State University/National Center for Atmospheric Research (PSU/NCAR) mesoscale model for numerically simulating the meso-β scale structure and evolution of convective weather systems, and 2) provide verification of the model simulation in order to

- establish credibility for the results of sensitivity and scientific experiments to be presented in subsequent parts of this series of papers, and
- demonstrate that the meso-β scale structure and evolution of mesoscale convective weather systems can be numerically simulated with sufficient skill to establish the *potential* for operational prediction of convective weather systems and for significant improvements in the warm-season QPF.

In the following section, the modified version of the PSU/NCAR mesoscale model used in the experiment is described. After the description of the model, initial data and initial conditions are briefly presented. Then the model-predicted results are compared with observational analyses by H78 and BS81. A summary and concluding remarks are given in the last section.

2. Model description

The basic governing system of the model is similar to that described by Anthes and Warner (1978). However, there are several important additions and improvements that have been incorporated for the present case study in order to better address the simulation of mesoscale convective weather systems. The most important contributions are the following:

- development and incorporation of a two-way interactive nested-grid procedure (see Zhang et al., 1986);
- incorporation of a modified version of the Fritsch–Chappell (1980a) convective parameterization into the fine-grid mesh (FGM) of the nested-grid model;
- incorporation of an R. A. Anthes/H. L. Kuo type convective parameterization into the coarse-grid mesh (CGM) of the nested-grid model (Anthes and Keyser, 1979);
- incorporation of a modified version of Blackadar's medium-resolution boundary-layer parameterization (Zhang and Anthes, 1982);
- incorporation of a one-way nesting type lateral boundary condition (Perkey and Kreitzberg, 1976) for the CGM outermost boundary; and
- incorporation of virtual temperature effects in the gas law.

The basic model features and parameter specifications are given in Table 1. The model contains 19 sigma levels. They are 0.9985, 0.977, 0.929, 0.873, 0.817, 0.761, 0.7045, 0.6475, 0.5705, 0.535, 0.4705, 0.41, 0.3505, 0.272, 0.2345, 0.178, 0.125, 0.075 and 0.025. The horizontal domain of the CGM covers 39×31 grid elements with center of 41°N, 80.5°W and the FGM has 43×37 elements with center at 41°N, 79.6°W. Figure 1 shows the nested-grid domains for the present study. The CGM ($\Delta x = 75$ km) and FGM ($\Delta x = 25$ km) terrain data are acquired from the NCAR thirty- and five-minute resolution tapes, respectively. The grid point values are obtained from a Cressman-type objective analysis technique; there is no smoothing of the raw interpolated values. The compatible CGM and FGM terrain information in the overlap region is obtained using the method described in Zhang et al. (1986) and Zhang (1985).

The use of virtual temperature is particularly important for studying moist convection since the usual existence of higher moisture content in lower levels will increase parcel buoyancy while low-level drying and upper-level moistening by convection tend to produce the virtual effect of low-level cooling and upper-level warming. A second significant reason to use vir-

TABLE 1. Summary of the nested grid model properties.

Model	Three-dimensional, hydrostatic, u, v, T, q and p_s predictive
Moisture cycle	Resolvable-scale and convective modules. Fritsch and Chappell scheme (1980a) plus convective adjustment for FGM, Anthes/Kuo scheme for CGM
PBL	Medium-resolution plume model, surface heating determined by surface energy budget with inclusion of moisture effect on solar insolation
Coordinate	$x, y, \sigma = (p - p_t)/(p_s - p_t)$ with Lambert map projection, p_t = 80 mb
Nesting	Two-way interactive in x, y with two separate dynamic interfaces
Numerical schemes	Second order spatial, Brown and Campana (1978) temporal differencing with Asselin (1972) filter; fourth order horizontal and implicit vertical diffusion
Lateral boundaries	One-way nesting for CGM, two-way interactive nesting for FGM
Grid dimensions	CGM: 39 × 31 × 19; FGM: 43 × 37 × 19
Grid increments	CGM: 75 km; FGM; 25 km
Time increments	CGM: 120 s; FGM: 40 s
Integration period	1200 GMT 19 July to 0600 GMT 20 July 1977
Average time	4.1×10^{-5} s on CRAY-1 (per time step per point)

tual temperature is because it substantially affects the calculation of geopotential height in the hydrostatic equation. Zhang (1985) has documented the model's sensitivity to the use of virtual temperature.

In the following subsections, we describe the basic modifications and improvements that have been done for the Fritsch–Chappell (FC) convective scheme and the Blackadar boundary layer scheme.

a. Convective parameterization

Because of the meso-β scale nature of warm-season precipitation patterns (McAnelly and Cotton, 1981; Kane et al., 1986), parameterizing some of the characteristics of individual convective clouds is essential. Fritsch and Chappell (1980a) assume that these characteristics can be determined from a cloud model and from the following three resolvable-scale parameters: available buoyant energy (ABE), vertical wind shear and vertical motion. They also assume that the effects of convective clouds on mass, moisture and momentum can be approximated on a grid length of about 20 km as if a single dominant cloud circulation consists of updraft, moist downdraft and induced environmental vertical motion. These subgrid components are computed using the condition that $\bar{M} = 0$.

After determining a convective time scale, τ_c, and the properties of the updraft, downdraft and compensating environmental motion, the local temperature tendency due to convection can be expressed in the following manner:

$$\left.\frac{\partial T}{\partial t}\right|_{\text{CONV}} = \frac{\bar{T} - T_0}{\tau_c}, \tag{1}$$

where

$$\bar{T} = a_u T_u + a_d T_d + a_e T_e, \tag{2}$$

$$a_u + a_d + a_e = 1. \tag{3}$$

The subscripts u, d, e represent updraft, downdraft and environment, respectively, and "a" denotes fractional area. This formulation includes the effects of both latent and sensible heating (see Zhang, 1985).

With this parameterization scheme and for idealized initial conditions, Fritsch and Chappell (1980b), Fritsch and Maddox (1981a,b) and Fritsch and Brown (1982) successfully simulated some observable features of MCSs using the Fritsch and Chappell (1980b) three-dimensional Cartesian coordinate model. However, when the FC scheme was applied to the present study, several aspects had to be modified for the scheme to be compatible with the PSU/NCAR model. Moreover, certain changes and improvements were made because of "real data" features not included in the tests of the FC scheme on the Fritsch et al. (1980) idealized initial conditions. These modifications are described as follows:

1) If the parcel is buoyant, the entraining plume properties (e.g., θ_e, u, v) are computed according to

$$\alpha'_u = \frac{\alpha_u M_u + \Delta M_u \alpha_0}{M_u + \Delta M_u}, \tag{4}$$

where α_u is the cloud property before mixing, α'_u after mixing and α_0 the environmental property. A constant

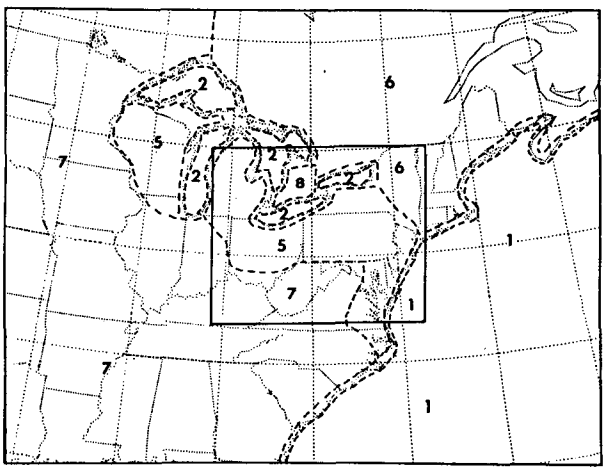

FIG. 1. Nested-grid domain with surface index distribution for present case study. The interior thick solid lines denote the mesh interface. Table 2 provides the values for the index (see section 2c for detailed description). Note that the transition zone between land and water surface (in which indexes 3 and 4 are used) is shown with double dashed lines.

entrainment rate ($\lambda = 6.5 \times 10^{-5}$ m^{-1}) is utilized rather than the bulk entrainment assumption, since the latter requires iterative computation which is time-consuming. The variation of mass flux with height is then given by

$$\frac{1}{M}\frac{dM}{dz} = \lambda. \tag{5}$$

2) The vertical velocities of the updraft and downdraft are calculated from

$$\frac{d\frac{w^2}{2}}{dz} = \frac{gB}{1+\beta} - \lambda w^2, \tag{6}$$

where the buoyancy term B is defined as

$$B = \frac{T_{vu} - T_{ve}}{T_{ve}}. \tag{7}$$

Note that the virtual temperature, T_v, and the effect of entrainment on cloud vertical motions are now included. Also, the "virtual mass" ($\beta = 0.5$), which partially compensates for the neglect of nonhydrostatic pressure perturbations, has been introduced. Since the computation of detailed microphysical processes is avoided in this scheme, the effect of precipitation drag is not included.

3) Instead of all moist downdrafts descending to the surface, parcels of downdraft air are now permitted to become buoyant as they encounter colder environmental air in their descent. At this point, their downward penetration is terminated.

4) Chen and Orville (1980) have shown that the magnitude of boundary-layer temperature and vertical motion perturbations is proportional to low-level convergence. Therefore, in their check for cloud-parcel buoyancy at the lifting condensation level (LCL), FC introduced a temperature perturbation, ΔT, which is a function of the resolvable-scale vertical motion at the LCL. Specifically, starting with the lowest 50 mb layer of air, successively higher 50 mb layers are mixed in the way

$$\bar{\alpha} = \Sigma\alpha\Delta z / \Sigma\Delta z, \tag{8}$$

and then lifted to the LCL where each layer is checked for buoyancy using

$$T_u(\text{LCL}) - T_{\text{LCL}} + \Delta T \begin{cases} >0, & \text{buoyant} \\ \leq 0, & \text{stable.} \end{cases} \tag{9}$$

The lowest layer which is buoyant at the LCL is used to construct the convective clouds. The temperature perturbation, ΔT, is computed from

$$\Delta T = C_1 w_{\text{LCL}}^{1/3}, \tag{10}$$

where C_1 is equal to 1.0°C s$^{1/3}$ cm$^{-1/3}$. The use of $w^{1/3}$ is an attempt to include the effect of large-scale forcing on the character of the subgrid-scale hygrotherms that are the "roots" of the convective clouds. As pointed out in the original FC paper, the width and amplitude of thermals seem to be proportional to the environmental forcing. As the forcing increases, the radius and amplitude (ΔT) of the "bubbles" also increases. This suggests a volumetric relationship—thus, the ⅓ exponent. The ⅓ exponent is also desirable since it easily accounts for the sign change as forcing switches to suppression. Observational studies, such as Lenschow (1970) and Bean et al. (1972) indicate that daytime perturbations are on the order of ±1 m s^{-1} or ±1°C in the boundary layer. For typical synoptic and mesoscale vertical motions, ΔT from Eq. (10) reflects these magnitudes, i.e., for $w_{\text{LCL}} = 0.01$ to 0.1 m s^{-1}, ΔT goes from 1° to 2°C. However, little is known about the diurnal variation of ΔT or if it is affected by such environmental parameters as wind shear, stability, etc. Observations of the diurnal variation of the organization of convective clouds into mesoscale convective systems suggest that daytime heating is disruptive to organization, and therefore convection is much more chaotic and widespread during the afternoon than at night (see Maddox et al., 1979; Caracena et al., 1979; Ward, 1981; Caracena and Fritsch, 1983). In particular, "air mass type" convection can be initiated in the afternoon due to local forcing in a well-mixed planetary boundary layer. This type of convection typically occupies relatively small areas for time periods much shorter than that of organized convective weather systems. Moreover, in real-data simulations, this type of convection can be spuriously triggered in models by the ever-present external gravity waves. In the Johnstown flood simulation, it was deemed desirable to filter out these spurious convective developments, as well as the physically real but less significant "air mass" elements, while retaining the areas of organized convection. Consequently, a time-dependent parameter, $C_2(t)$, is introduced into Eq. (10) to damp spurious initiation of convection when the boundary layer is well mixed but environmental forcing is weak or negative. The perturbation equation then becomes

$$\Delta T = C_1[w_{\text{LCL}} - C_2(t)]^{1/3}. \tag{11}$$

Figure 2 shows the portion of the diurnal distribution of $C_2(t)$ used for the Johnstown flood simulation.

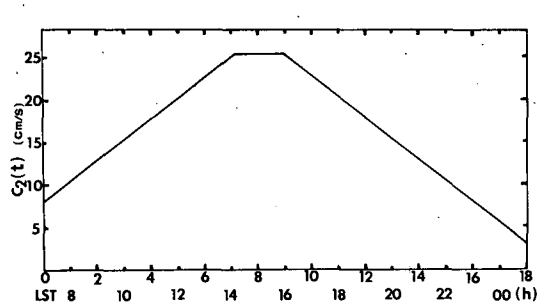

FIG. 2. Diurnal perturbation filter, $C_2(t)$, from Eq. (11). Filter shown as a function of model and local standard time (LST).

5) One important closure assumption for computing the amount of precipitation in this scheme is to relate the precipitation efficiency (E) to the vertical wind shear. The stronger the wind shear, the less efficient are the convective clouds and more condensate is lost to evaporation in the moist downdrafts. Therefore, the way in which wind shear is computed can alter the partitioning of condensate into downdraft, anvil evaporation and convective precipitation. This, in turn, affects the vertical distribution of convective heating. Moncrief and Green (1972) and Weisman and Klemp (1982) used wind information at low and middle levels to define the wind shear. Correspondingly, the wind shear between the LCL and the maximum wind level at least 300 mb above the LCL is employed here to compute precipitation efficiency, instead of the shear over the total cloud depth as originally used by FC. In addition to the effect of the wind shear, some evidence indicates that the precipitation efficiency can be affected by the height of cloud base (Fujita, 1959; Braham, 1952). Intuitively, the higher the cloud base, the more condensate should evaporate, and less precipitation reaches the ground. Hence, a relation based on observation (Fig. 13 in Fujita, 1959) is also used to compute E. This relation is given by

$$E_{CB}=\frac{1}{1+E_R}, \tag{12}$$

where

$$E_R=0.967-0.700Z_{\mathrm{LCL}}+0.162\,Z_{\mathrm{LCL}}^2 - 1.257\times10^{-2}\,Z_{\mathrm{LCL}}^3, \tag{13}$$

and Z_{LCL} is the height of the LCL in units of thousands of feet. Then the mean of this estimated efficiency and the one obtained from the vertical wind shear relationship is used in the model calculations.

6) Rather than the mean wind over the total cloud layer, the mean wind in the layer from the LCL to 300 mb above the LCL is used to calculate the convective time scale τ_c.

7) Finally, the magnitudes of convective heating, moistening and momentum exchange are determined by the closure assumption that convective clouds can only remove 50% of existing ABE during the convective time period, τ_c.

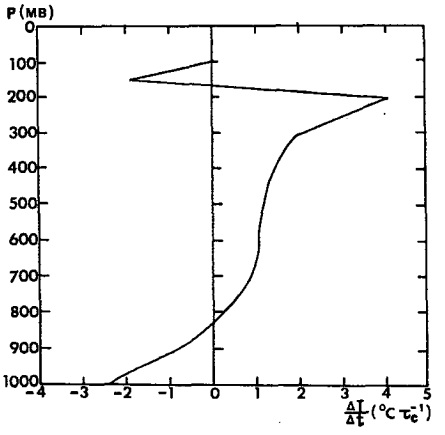

FIG. 3. A typical convective heating profile (°C τ_c^{-1}) produced by the Fritsch–Chappell cumulus parameterization scheme for the present case study.

Figure 3 shows a typical convective heating profile generated by the FC scheme *in this case study*. This profile is different from other heating profiles (e.g., Anthes, 1977; Kuo, 1965, 1974) with respect to the high level of maximum heating and, in particular, the low-level cooling. In the FC scheme, such a profile is typical for *intense* convective storms with very strong updrafts. For environments in which the updrafts are relatively weak, such as in many tropical convective clouds, the level of maximum heating tends to occur at a much lower level. Moreover, the vertical wind shear tends to be less and cloud bases lower in the tropics than in the midlatitudes, so cooling by moist downdrafts tends to be greater over midlatitude land areas in the FC scheme. Physical processes involved in producing the Fig. 3 profile are as follows. Buoyant parcels release latent heat as they rise through a conditionally unstable environment. After reaching the equilibrium temperature level, the parcels overshoot and detrain into the stable environment in the vicinity of the tropopause. Cloud condensate is also detrained in this region so that evaporation in the overshooting parcels results in cloud-top cooling. Because of mass conservation, updraft-induced subsidence brings potentially warmer environmental air downward, thereby generating the strong warming at upper tropospheric levels. Meanwhile, moist downdrafts initiated at the level of free sink penetrate into the PBL and fill it with air of low moist static energy.

Because of the strong gradient of $\partial T/\partial t|_{\mathrm{CONV}}$ at upper levels (see Fig. 3), a dry convective adjustment described by Anthes and Warner (1978) is performed for layers above 500 mb. This is a necessary step since the FC scheme sometimes imposes a superadiabatic heating/cooling rate profile in the upper levels and under certain environmental conditions this might lead to numerical instability. Experimentation with the modified FC scheme indicated that the dry convective adjustment is only needed when the intense convective overturning occurs continuously at the same grid point for several hours. On the average, the number of grid points at which the adjustment was needed was less than 5% of the total grid points at which the model convection occurred at each time step. And in regions when the convection was not particularly intense, no adjustments were necessary. It is possible that the adjustment procedure may not be needed if the model resolution were increased at upper levels and/or a higher model top (lower pressure) were introduced.

Furthermore, inclusion of precipitation drag would likely reduce the magnitude of the heating and lower the level of maximum heating. Still further, the compensating subsidence (which is primarily responsible for the strong heating at high levels) could be spread over greater areas, i.e., in grid elements adjacent to the elements where convection is occurring. This would reduce the heating *rates*. Fritsch and Chappell (1980a) considered this possibility when designing the original parameterization scheme. However, the problem with this approach is that there is no information to tell how to distribute the subsidence, i.e., how much goes to which grid elements? Thus, it is deemed better to assume that the effects of the convection first occur locally (based on Lilly, 1960; Fritsch, 1975; Lipps and Hemler, 1985). In this manner, the effects are introduced in the same grid element where the convection is occurring and then the mesoscale governing equations distribute the effects in a manner that would account for whatever the particular environmental conditions warrant. Thus, in some cases, the effects of the convection are "felt" uniformly around the convection while in other situations (e.g., with strong shear) the effects are distributed very asymmetrically.

b. *Boundary-layer parameterization*

To provide a more accurate and efficient simulation of PBL processes, the previous PBL parameterization procedure (Zhang and Anthes, 1982) has been modified and streamlined. It is now two to three times faster than before. More important modifications are made in the computation of the surface energy budget. This budget is described by

$$C_g\frac{\partial\theta_g}{\partial t}=R_n-H_m-H_g-H_l+\left.\frac{\partial\theta_g}{\partial t}\right|_{\text{CONV}}, \qquad (14)$$

where R_n denotes the radiative flux, H_m the heat transfer into the ground, H_g the upward sensible heat flux and H_l the latent heat flux. The term $\partial\theta_g/\partial t|_{\text{CONV}}$ refers to the ground potential temperature tendency due to moist convection. The same $\partial T/\partial t|_{\text{CONV}}$ produced by the FC scheme for the first model layer ($\approx$15 m above the ground) is utilized to derive $\partial\theta_g/\partial t|_{\text{CONV}}$. Basic changes in Eq. (14) and others are listed below.

1) Radiative flux, R_n, has been modified by Benjamin (1983) to include some of the cloud effects from the following physical processes:

- Shortwave radiation depends upon attenuation by water vapor, clouds, Rayleigh and aerosol scattering, and multiple reflection between the surface and atmospheric scatterers.
- Downward longwave radiation reaching the ground depends on the low-level atmospheric temperature, clouds and the precipitable water in an atmospheric column.

2) Latent heat flux, H_l, is computed following Carlson and Boland (1978). This scheme assumes a near-surface molecular layer, z_l, with a depth of 1 cm over land. In this layer, molecular diffusion equals turbulent transfer. The latent heat flux is calculated from

$$H_l=L_vQ_g=A_m\rho L_vI^{-1}(q_s(T_g)-q_a), \qquad (15)$$

where

$$I=\int_0^{z_l}\frac{dz}{k_{qt}+k_{qm}}+\int_{z_l}^{z_a}\frac{dz}{k_{qt}}$$
$$=\frac{1}{ku^*}\left[\ln\left(\frac{ku^*z_l+k_{qm}}{k_{qm}}\right)+\ln\frac{z_a}{z_l}-\psi_h\left(\frac{z_a}{L}\right)\right] \qquad (16)$$

and A_m is the moisture availability with a span from zero for dry land to one for water surface. All other symbols assume their usual meteorological meaning.

3) The PBL package described by Zhang and Anthes (1982) only applies over land. Application over water surfaces is determined as follows:

- the water surface temperature is assumed to be constant rather than predicted from (14);
- the latent heat flux from the water is calculated using (15) and (16), but with roughness length given by

$$z_l=z_0=0.032u_*^2/g+z_{0b} \qquad (17)$$

where z_{0b} is a background roughness length of value 10^{-4} m (see Delsol et al., 1971). Utilization of (15) and (16) is equivalent to applying the surface resistance law. In the present simulation, the resistance γ is introduced in a series configuration, consisting of the molecular layer and the surface layer, rather than in parallel as in Westphal (1981). Therefore, the resistance is given by

$$\gamma=\gamma_1+\gamma_2, \qquad (18a)$$

$$\gamma_1=\ln\left(\frac{ku^*z_0}{k_{qm}}+1\right)\Big/ku^*, \qquad (18b)$$

$$\gamma_2=\left[\ln\frac{z_a}{z_0}-\psi_h\left(\frac{z_a}{L}\right)\right]\Big/ku^*. \qquad (18c)$$

The sensible heat flux, H_g, and moisture flux, Q_g, from the water surface are calculated from

$$H_g=\rho C_p(T_g-T_a)/\gamma, \qquad (19a)$$

$$Q_g=\rho(q_s(T_g)-q_a)/\gamma, \qquad (19b)$$

respectively.

4) To be consistent with other portions of the model, the potential temperature, θ, in Zhang and Anthes (1982) is replaced by virtual potential temperature, $\theta_v=\theta(1+0.608q)$, except at the ground where the mixing ratio is not available.

5) Because of the very thin surface layer ($\Delta z\approx$ 20–30 m), an iterative technique is required in Zhang and

Anthes (1982) to obtain surface tendencies. This is very time consuming. In this study, the iterative calculation for stable conditions is eliminated by setting a limit on the K coefficient and therefore the computational stability requirement is satisfied. If a superadiabatic lapse rate develops between the surface layer and the layer above, the Priestley equation [see Eq. (30) in Zhang and Anthes, 1982] is used to compute the surface heat flux. For unstable conditions, an analytic solution developed by Blackadar (personal communication, 1982) is utilized to calculate the surface tendencies (see Zhang, 1985).

6) Turbulent transfer under stable conditions largely depends on the magnitude of the K-coefficient,

$$K = K_0 + \left|\frac{\partial \mathbf{V}}{\partial z}\right|(kl)^2(R_c - \mathrm{Ri})\Big/R_c. \tag{20}$$

In this formulation, specification of the critical Richardson number, R_c, is important. Shir and Bornstein (1977) noted that the value of R_c must increase with layer thickness in order to obtain reasonable K profiles. Thus, following McNider and Pielke (1981), R_c is related to the model grid spacing by the expression

$$R_c = A(\Delta z)^B \tag{21}$$

where Δz is in meters, $A = 0.257$ and $B = 0.175$. In the surface layer, we still use the value of 0.25 for R_c.

7) The original formulation in Blackadar (1978) and Zhang and Anthes (1982) to compute the convective mixing between the surface layer and the layer above tends to produce a uniform mixed layer of virtual potential temperature, momentum and mixing ratio. As a consequence, large and sometimes unrealistic vertical gradients can develop at the top of this mixed layer after sunset. Since the lifted condensation level is sensitive to small changes in moisture and since the sharp gradients in momentum may sometimes produce spurious vertical circulations, the initiation and evolution of deep convection can be significantly, but artificially, affected. Thus, a weighting factor, suggested by Estoque (1968), is applied to the momentum and moisture tendencies. Specifically,

$$W(z) = 1 - z/z_h, \tag{22}$$

$$\frac{\partial \alpha_k}{\partial t} = \bar{m} W(z)(\alpha_a - \alpha_k), \tag{23}$$

$$\frac{\partial \alpha_a}{\partial t} = -\left(F_g/\rho - \sum_{k=2}^{h} \frac{\partial \alpha_k}{\partial t}\Delta z\right)\Big/z_1, \tag{24}$$

where α denotes u, v or q, z_h is the height of the mixed layer, z_1 is the thickness of surface layer, $\bar{m}$ is the fraction of mass exchange between any level and the surface layer per unit time, F_g represents fluxes from the ground, and subscripts a and k denote surface layer and the level in the mixed layer, respectively. The inclusion of the weighting factor significantly reduces the vertical gradient at the top of the mixed layer and provides more realistic vertical profiles. Blackadar (1978) noted, however, that the potential temperature distribution is relatively insensitive to the weighting function.

TABLE 2. Surface parameters assigned to the surface index.

Surface index	Moisture availability, A_m	Roughness length, z_0 (m)	Albedo, A	Thermal potential C_g ($\times 10^5$ J m^{-2} K^{-1})
1	1	10^{-4}	0.25	2.5
2	0.85	10^{-3}	0.25	2.5
3	0.7	0.05	0.25	2.2
4	0.6	0.1	0.25	1.8
5	0.5	0.5	0.25	1.2
6	0.4	0.5	0.25	1.0
7	0.4	0.8	0.25	1.0
8	0.5	0.3	0.75	1.4

c. *Spatial variation of surface parameters*

Surface parameters, such as moisture availability, roughness length, albedo and thermal potential, significantly affect the energy input into the model atmosphere, particularly the vertical partitioning of energy in the lower troposphere. Numerous studies (e.g., McCumber and Pielke, 1981; Carlson and Boland, 1978; Zhang and Anthes, 1982) have indicated that the development of the planetary boundary layer is very sensitive to these surface parameters. Moreover, it is important to resolve their spatial variability and to properly permit the evolution of the PBL under different meteorological conditions. Therefore, surface parameters used in this study are allowed to vary horizontally over the model domain (see Fig. 1). A surface index describing these parameters is assigned to each grid point; this is accomplished with the use of a look-up table (see Table 2).

The values for these surface parameters are determined from Sellers (1965), Kondratzev (1969) and sensitivity tests in Zhang and Anthes (1982). The surface index in Fig. 1 was basically derived from surface features (e.g., land or water, mountain or flat surface, etc.), visible satellite images and the history of precipitation evolution, with more detail provided in the FGM than the CGM. For example, during the first 7–8 h of integration of the Johnstown flood event, the corresponding satellite images show a large area of stratocumulus over Ontario, Canada. Since the cloud shading of solar insolation cannot be adequately accounted for by the radiation scheme described in section 2b, a value of 0.75 for albedo is used for that region until the eighth model hour. After that time, a value of 0.25 is used. It was found during the initial testing stage that such specification tends to improve the surface temperature forecast over that region, but does not significantly affect the general events in this study. In a second example, when moist convection is taking

place at a grid point, the solar insolation is shut off and the maximum value between the assigned value and 0.75 is used for moisture availability A_m. Furthermore, the albedo (A) is set to 0.75 and moisture availability to 0.60 during the 1-h period after convection ceases at a grid point (over land). In yet a third example, a transition zone with an increase of roughness length toward land is utilized at the interface between water and land in order to avoid the resulting irregular flow when a discontinuity in roughness length is introduced.

Despite its simplicity, this method enables the capture of basic differences in the PBL development between land and water surfaces, dry and moist ground, clear and cloudy skies, etc., and thus permits a reasonable simulation of the horizontal pattern of the PBL development for the case study.

3. Initial data and initialization

a. Data sources and processing

It has been increasingly recognized that without the proper initial conditions, the development of mesoscale features within a model is subject to large errors in timing, location and magnitude (see Perkey, 1976; Kelly et al., 1978; Chang et al., 1984; Anthes et al., 1981). This sensitivity is also present in this study of the Johnstown flood since numerical experiments indicated that observations from central Ohio and central Pennsylvania were crucial in determining the evolution of the convective systems. Yet, if only objective analyses were used for initialization, the model grid point information would be determined entirely from weighted averages of *adjacent* observations. This procedure, as shown by Barnes (1974), may miss important mesoscale features that could later affect the model forecast of mesoscale circulations. In addition to the lack of direct observations over central Ohio and Pennsylvania, there were no upper air observations over Lake Erie where the convective system was initially developing. Therefore, it is desirable to introduce initial conditions which include mesoscale features detectable in satellite and radar data and apparent from careful subjective analysis. To do this, one has to invoke artificially constructed, or simulated soundings. For this case study, it is very fortunate that a well-documented dataset developed by L. F. Bosart (personal communication, 1982) is available. This dataset contains temperature, dewpoint depression and horizontal wind components every 100 mb from 1000 to 100 mb with one-degree latitude–longitude resolution over the FGM domain. In addition to eight conventional rawinsonde observations in the FGM domain, thirty soundings were selected from Bosart's analysis to aid in resolving mesoscale features. No soundings from Bosart's analysis were introduced into the CGM domain except in the region that is common to both the fine mesh and coarse mesh.

In order to improve the quality of initial data, soundings from Bosart's analysis are adapted to incorporate information at some significant levels, especially the inversion and observed surface data (see Zhang, 1985 for details).

b. Initialization

The nested-grid model is initialized using the technique described by Zhang et al. (1986) and Zhang (1985). Briefly, the procedure begins by specifying the CGM condition using the National Meteorological Center (NMC) analysis as a first guess and then enhancing this analysis with the available soundings. The FGM was initialized using the enhanced CGM-interpolated values as a first guess and then enhancing these values using the observed soundings and the soundings from Bosart's analysis. No balancing between mass and wind fields is performed. However, the vertically integrated divergence in a column is removed from the wind field (Washington and Baumhefner, 1975) in order to minimize noise early in the forecast. The surface pressure at grid points is computed from the hypsometric equation using information from surface observations (see Zhang, 1985 for details).

c. Initial conditions

Because the long-lived MCC responsible for the Johnstown flood produced 200–300 mm of rain over an 8 to 9 h period, resulting in the loss of 77 lives and more than $200 million in property damage, several synoptic and mesoscale analyses of the event were quickly completed. The first study, by H78, focused on the mesoscale structure and evolution of the storm and its large-scale environment during the 24 h period

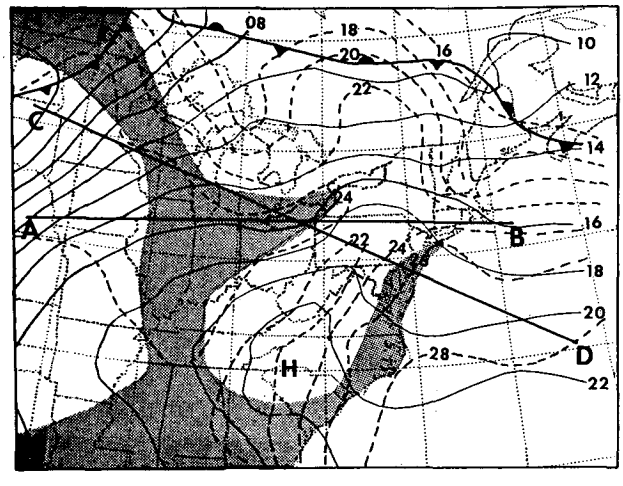

FIG. 4. Surface synoptic analysis for 1200 GMT 19 July 1977. Solid lines are sea level isobars (mb) and dashed lines are isotherms (°C). Shading denotes area (over land) of mixing ratio exceeding 16 g kg^{-1}.

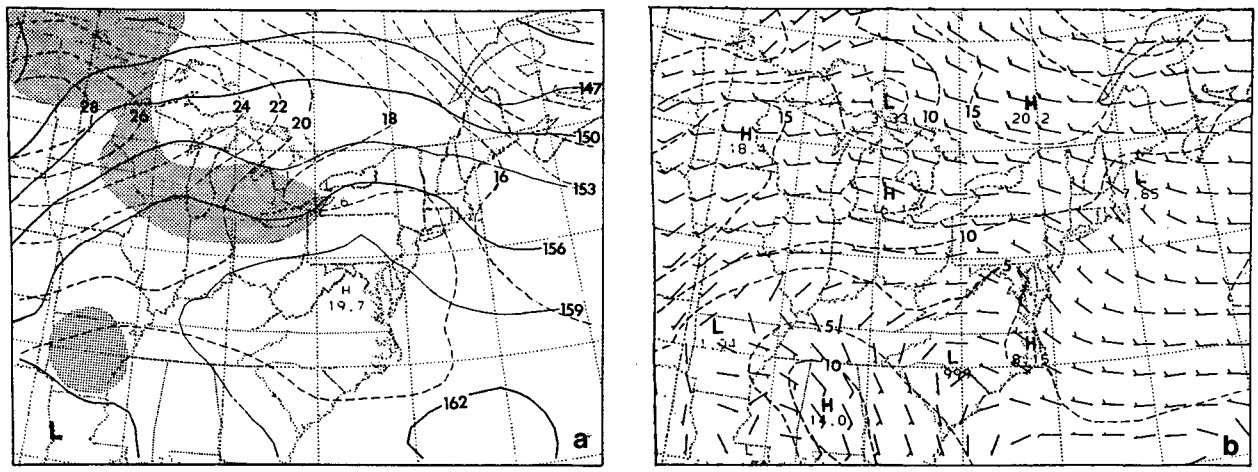

FIG. 5. 850-mb synoptic chart for 1200 GMT 19 July 1977. (a) Height in dam (solid lines), temperature in °C (dashed lines). Shading denotes area of dewpoints exceeding 17°C. (b) Wind speed in m s^{-1} (dashed lines). A full barb is 10 m s^{-1}.

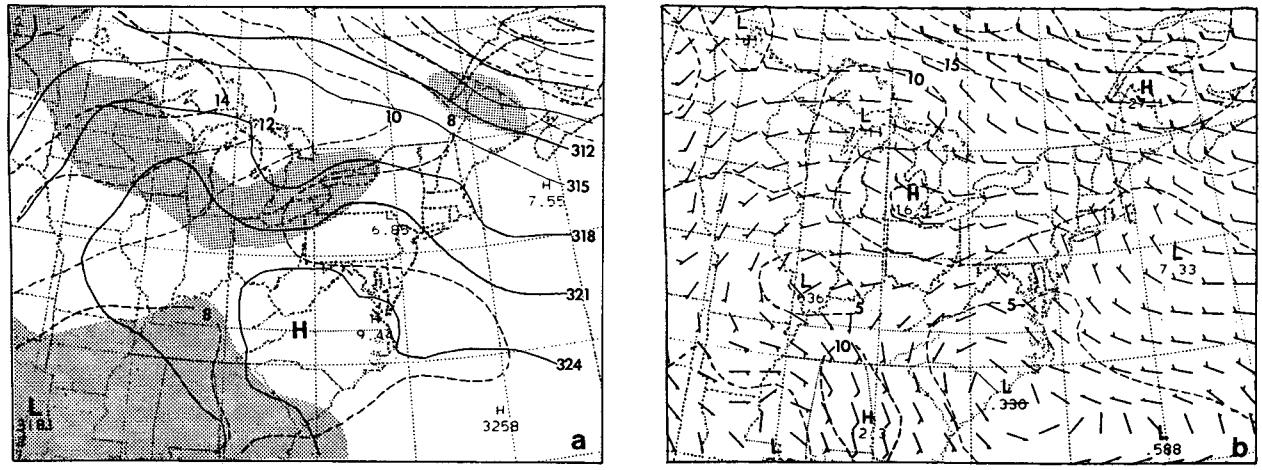

FIG. 6. As in Fig. 5 but for 700 mb analysis. Shading denotes area of dewpoints exceeding 3°C.

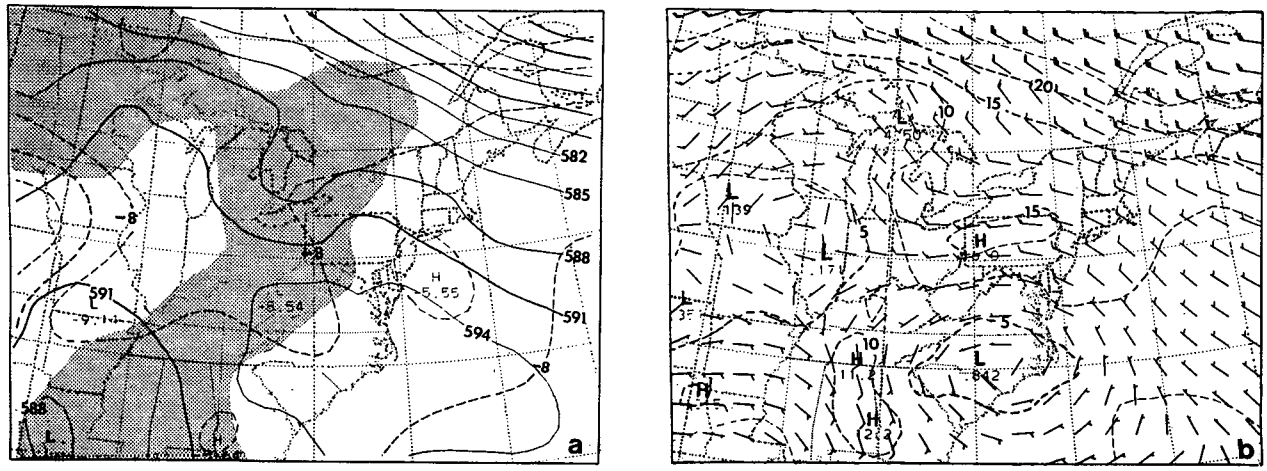

FIG. 7. As in Fig. 5 but for 500 mb analysis. Shading denotes area of dewpoints exceeding −12°C.

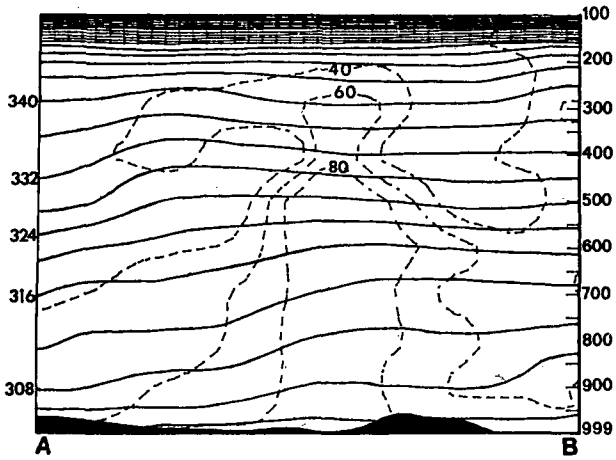

FIG. 8. Cross section along line AB in Fig. 4. Solid lines denote potential temperature in K and dashed lines indicate relative humidity (%). The scalloped area is terrain.

encompassing the flooding events. This study is particularly useful for comparison to the mesoscale model output since it provides an hourly evolution of the movement of the rain areas (radar summaries) along with the corresponding evolution of the meso-β scale pressure systems. In a later study, BS81 traced the convective complex back to its origin in South Dakota nearly 96 h earlier and examined the mesoscale environment within which this complex evolved over the four-day period. The BS81 study presented evidence for the existence of a convectively generated warm-core vortex—a feature which turns out to be extremely important to the successful simulation of the heavy rain event.

Since these two studies are available in the literature, only a brief description of the large-scale and mesoscale conditions for the organization of the convective events will be presented here. In the next section, the model-predicted dynamical and thermodynamical evolution of the convective systems will be described in detail and compared sequentially to the surface and upper-air analyses from H78 and BS81.

Figures 4–9 show the synoptic conditions at 1200 GMT 19 July 1977. This is approximately the time of initiation of deep convection; it is also the model initial time. Note that the Bosart soundings within the FGM are included in Figs. 4–9. From Fig. 4, it is apparent that most of the eastern United States is dominated by anticyclonic flow around a large subtropical high. Because of this feature, there is a continuous flow of warm, moist air into the mid-Atlantic states. Correspondingly, the polar jet is far to the northwest, as evidenced by the frontal systems extending from eastern Canada to the northern high plains of the United States. A sea-level pressure perturbation associated with a short wave aloft is evident in the vicinity of eastern Michigan, Ohio and northwestern Pennsylvania. It is this mesoscale feature that is largely responsible for initiating and maintaining the convective systems in the following 24 h. Associated with this short wave is a pool of cool air in the lowest 100–200 mb of the troposphere (see Figs. 4 and 5), while strong warm advection is occurring behind the short-wave trough over the Lake Huron and Lake Erie region (Figs. 5 and 6). In the face of this warm advection, the cool pool slopes southeastward with height. Its center is near the surface over northern Michigan and then rises to approximately 700 mb over eastern Pennsylvania. Above 700 mb, there is little horizontal temperature advection except in the west and north near the synoptic-scale frontal system. The southeastward slope of the cool pool, along with the rapid reversal of the meridional temperature gradient with height over the central Great Lakes region, seem to be very important to the explosive development and persistence of deep convection over Lake Erie and northwestern Pennsylvania later on. Specifically, from thermal wind considerations, the rapidly reversing thermal gradient corresponds to a low-level (900–850 mb) westerly jet overlain by relatively weak winds. Conversely, farther to the east, the strongest winds occur at significantly higher levels (600–400 mb, see Fig. 9). Therefore, such a thermal pattern results in low-level convergence and upper-level divergence in the vicinity of Lake Erie and northwestern Pennsylvania. Furthermore, when coupled with the fact that the low-level air from the west and northwest was exceptionally warm and moist, the potential for deep convection was high (see Figs. 8 and 9). Studies by BS81 suggest that the low-level convergence feature and the tilting of the cool pool with height were produced, one way or another, by convection that occurred on previous days as the disturbance propagated toward Pennsylvania.

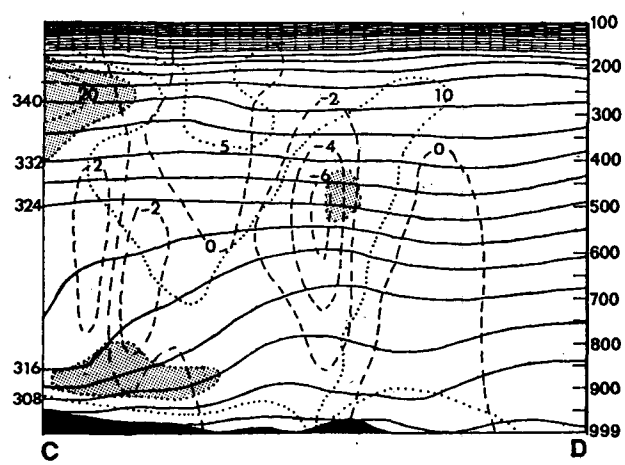

FIG. 9. Cross section along line CD in Fig. 4. Solid lines are potential temperature in K and dashed lines are ω in μb s^{-1}. The dotted lines denote wind speeds in m s^{-1}; speeds greater than 15 m s^{-1} are shaded. The scalloped area is terrain.

4. Numerical model simulation

This section presents the results from an 18 h numerical simulation of the Johnstown flash flood. In order to help evaluate model skill in simulating the evolution of the various mesoscale convective systems responsible for the flood, the model results are compared to the well-documented diagnostic analyses of H78 and BS81. To clearly show important meteorological events and flow patterns of different scales, sections 4a and 4b present the meso-β and α scale structure and evolution of the MCSs in the FGM framework while section 4c describes the large-scale aspects from the CGM framework.

a. Simulation of the mesoscale evolution of surface features

According to BS81, the MCS responsible for the Johnstown flood had undergone four diurnal cycles wherein it tended to become more compact and intense during the nighttime and expand in response to the mixed-layer development during the day. However, during the period 0000–0900 GMT 19 July, the MCS was in its weakest and least coherent state since its initiation in South Dakota. The nocturnal compacting that appeared in preceding nights did not occur during this period. Even at 0900 GMT 19 July (see Fig. 10), no deep convective activity is apparent in the enhanced infrared satellite image except for a few small areas in southeastern Michigan. However, at the model initial time (1200 GMT), satellite imagery shows that a new and significant area of deep convection developed over Lake Erie (see Fig. 10). The size and location of this new area of convection is very closely approximated by the model at the first time step (Fig. 11a) and during the subsequent 1–3 h model adjustment period. The closed dot–dashed line within the MCS in Fig. 11a is the 1014 mb isobar from the BS81 analysis. This feature is not explicitly included in the model initial conditions since no upper-air data were available at that location. Nevertheless, it is included in Fig. 11a since the model integration (described below) tends to support its existence. Other important features apparent in the model initial analysis are the westerly wind maximum and high-θ_e distribution nearly coincident with the MCS, the ridge of cool and dry air over the Appalachians, and the high-θ_e air flowing into Pennsylvania from the west.

Three hours after the initial time, the MCS has organized into a vigorous squall line with southwest–northeast orientation (see Fig. 10). At the surface (Fig. 12), a large amplitude pressure perturbation associated with the MCS has developed. The location of the pressure trough appears to be in reasonable agreement with the position of the low analyzed by BS81. In addition to the low-pressure perturbation, moist downdrafts from the deep convection apparently were responsible for the development of a surface mesohigh at the southwestern end of the MCS and a ridge over western New York and northwestern Pennsylvania. The moist downdrafts produced a cool pool along the axis of the MCS while, in contrast, strong solar heating warmed surface air adjacent to this region by 4°–6°C and surface evaporation increased dew points by 1°–2°C. Thus, a strong temperature gradient is present around the "model cloud" boundary.

Figures 13a–d show the observed and predicted surface features at 1800 GMT. This is a crucial time in the integration since at this time the squall line continues eastward and separates from the convection over northwestern Pennsylvania. Such meso-β scale storm splitting also occurred in a mesoscale convective system studied by Smull and Houze (1985). The model, surprisingly enough, simulates the separation of the squall line from the original area of convection (hereafter referred to as the MCC since it later developed into the MCC responsible for the major flood event). Moreover, the model-predicted separation occurs at approximately the right location and right time when compared to the observations. In fact, it is readily apparent by comparing Figs. 13a and 13c that the basic configuration and locations of deep convection are well simulated except for the slight southwestward extension of the squall line. Furthermore, the surface ridge–trough system and location of the mesohigh accompanying the squall line conform exceedingly well to the H78 analysis. Of particular interest is the relative position of the squall line with respect to the ridge–trough system. Note that the convection did not initiate along the trough axis but rather some distance behind it. This is an indication that internal gravity waves may have been excited by the squall line and are now interacting with the convection (Eom, 1975; Uccellini, 1975; Zhang, 1985).

It is also evident that, in the model, the pressure trough centered over Lake Erie three hours ago has evolved into a closed meso-β scale low as strong as that analyzed by BS81 for 1200 GMT, although H78's analysis only shows a deep trough. This discrepancy may be due either to the poor resolution of the surface observations or an overprediction of the low's central pressure. Note that there is a warm-core mesovortex, corresponding to the mesolow, in the low- to midtroposphere (see Zhang and Fritsch, 1985). To the west and northwest of the squall line and MCC, the surface pressure perturbations are reasonably consistent with observations. The trough extending from the Great Lakes southward into Ohio seems to correlate well with the edge of the cool surface air. While the cool air over Pennsylvania resulted primarily from moist downdrafts, to the north the cool ridge over Ontario, Canada, resulted from cloud shading and a lake effect. Unlike for the convection, the cloud cover in this region was

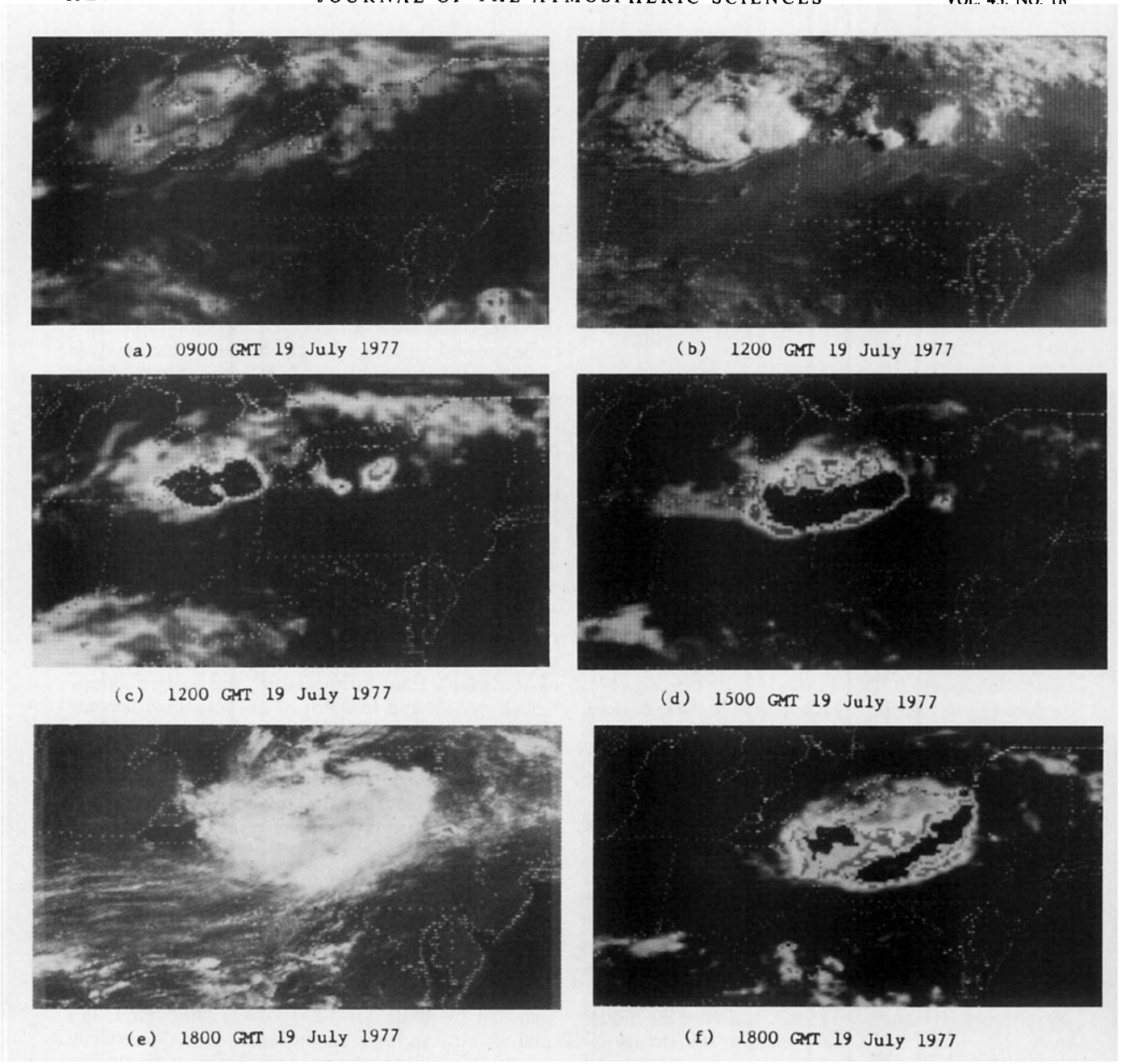

FIG. 10. GOES-1 visible and infrared satellite imagery for times indicated.

specified (in the model) based on the observed cloud distribution (see section 2c). Up to this point in the simulation, and throughout the remainder of the simulation, the greatest and most obvious departure of the model-predicted pressure field from the "observed" occurs over West Virginia. A narrow, but strong ridge oriented along and coincident with the axis of the Appalachians persists through the duration of the integration period. While the model does indicate the maintenance of a ridge in approximately the same location, the magnitude is considerably less. Note, however, that absolute comparisons of *sea level* pressure between forecasts and observations are difficult since reported values are *derived* from a weighted temperature average of a *6 h interval* while the model initial and predicted values are determined from temperature at that instant of time.

In addition to the surface pressure features and the configuration of the convection, it is also important to examine the thermal and moisture fields. The surface

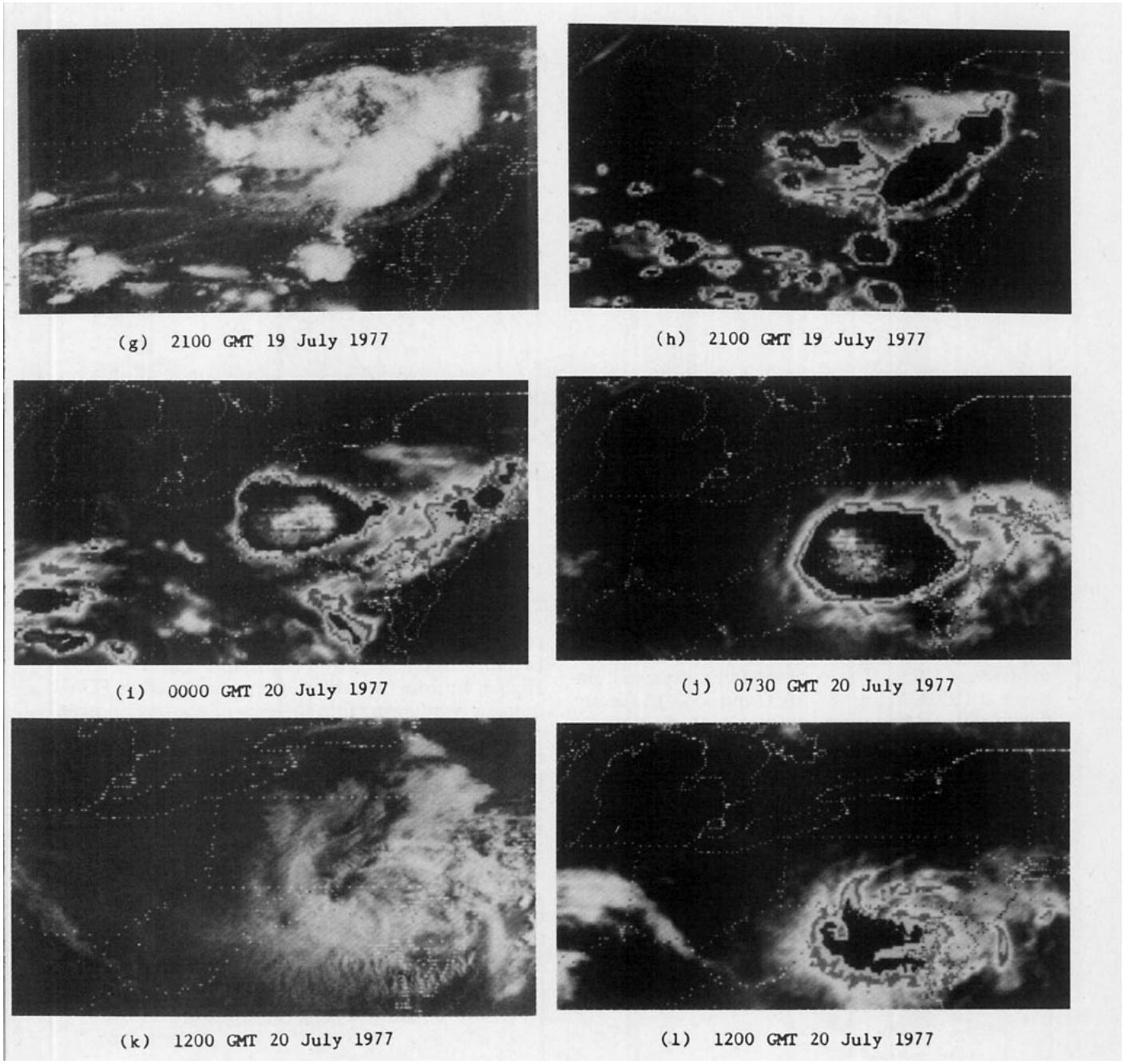

FIG. 10. (*Continued*)

temperatures and dew points under both clear air and cloud shields compare well to the surface reports. For example, the observed temperature and dew points over Ohio have respective values of 32°–33°C and 22°–23°C in comparison to the predicted values of 30°–31°C and 22°–23°C, while underneath the MCC (northwestern Pennsylvania) observations show 21°C temperature and 20°C dew points compared to the predicted 22°C. This is particularly encouraging considering that the predicted surface temperatures are extrapolated downward from the first model level ($\approx$15 m) by assuming the standard lapse rate. Thus, 1°–2°C underestimations can be expected for daytime situations in which superadiabatic lapse rates occur, and 1°–2°C overestimations can be expected for strong inversion situations. Of course, this can not explain the 2°–4°C temperature differences along the east coast. On the other hand, the model simulates the observed

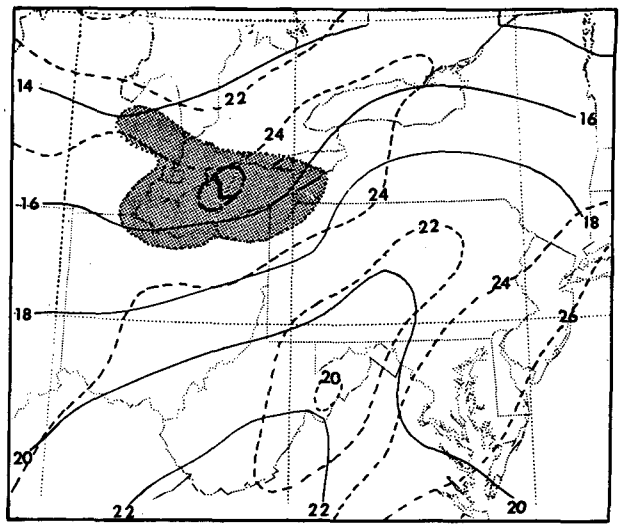

FIG. 11a. Analysis of sea-level pressure (solid lines, mb) and surface temperature (dashed lines, °C) at 1200 GMT 19 July 1977. Shading denotes the area of active convection. Dot-dashed line indicates isobar from BS81's analysis.

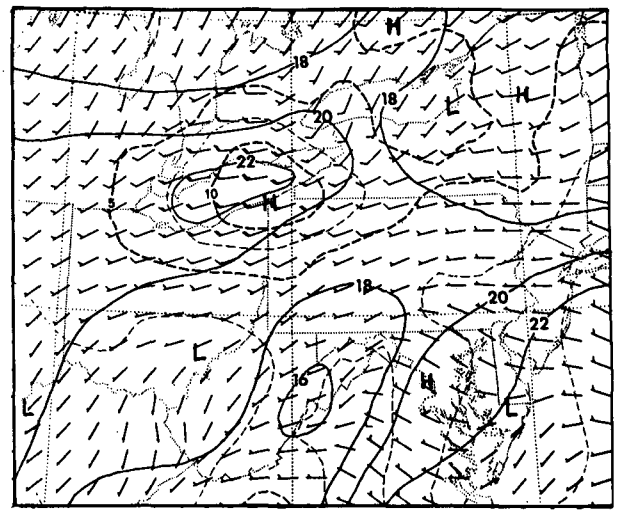

FIG. 11b. Analysis of surface wind (dashed lines, m s^{-1}) and surface dewpoint (solid lines, °C) at 1200 GMT 19 July 1977. A full barb is 5 m s^{-1}.

temperature and moisture *gradient* reasonably well. Temperature and dew point gradients as strong as 6°–8°C and 4°C, respectively, are produced across the model squall line. The corresponding observed gradients at 1800 GMT are 8°–10°C and 3°–5°C. Clearly, this strong cool boundary has important effects on the structure and propagation of the squall line (Matthews, 1981; Weaver and Nelson, 1982), as evidenced by the arc cloud well ahead of the squall line during 1800–2100 GMT (see satellite images in Fig. 10). Another particularly interesting feature is the correlation between surface flow and θ_e distribution (see Fig. 13b). High-θ_e air from the northwestern portion of the FGM domain was flowing into the area of convection over northeastern Ohio and northwestern Pennsylvania. A narrow west-southwesterly air stream transported the high-θ_e air ahead of the model squall line while a broad westerly air stream brought high-θ_e into the MCC surroundings. To the east of the Appalachians, southwes-

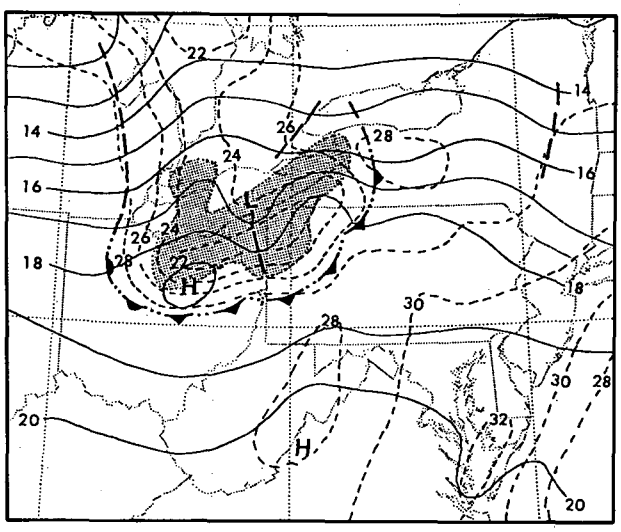

FIG. 12a. Analysis of sea-level pressure (solid lines, mb) and surface temperature (dashed lines, °C) for 3 h forecast verifying at 1500 GMT 19 July 1977. Heavy dashed lines indicate troughs. Cold and warm-frontal symbols alternated with double dots indicate moist-downdraft outflow boundaries. Shading indicates area of active convection at verification time.

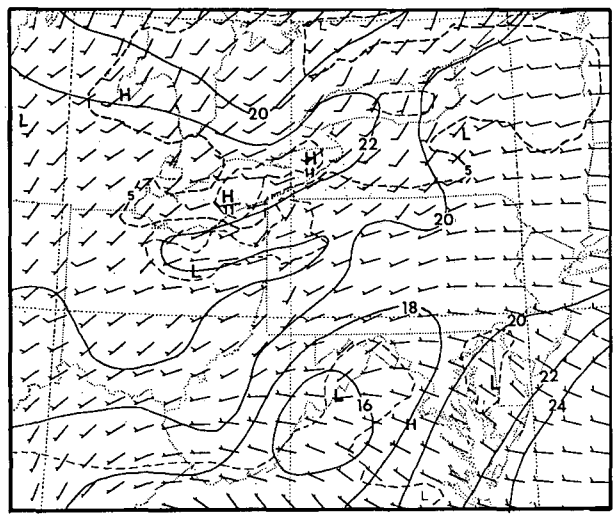

FIG. 12b. As in Fig. 11b but for 3 h forecast verifying at 1500 GMT 19 July 1977.

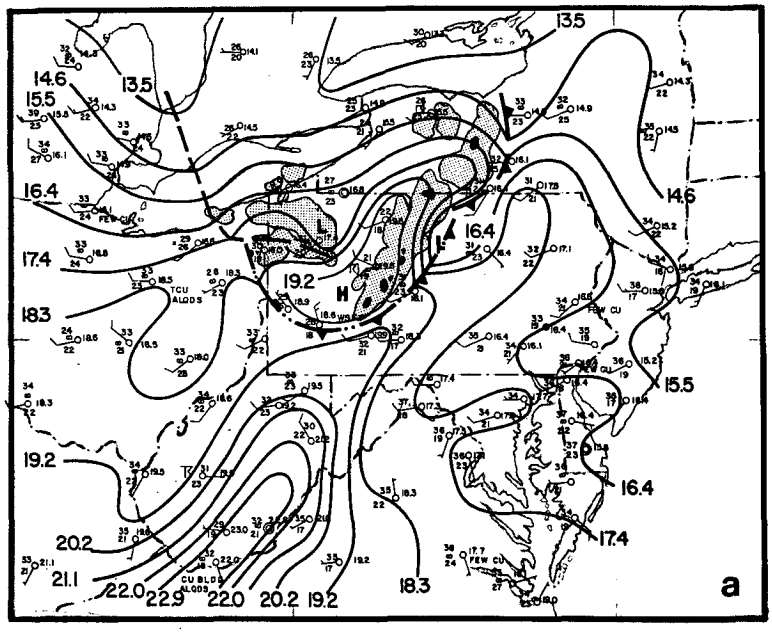

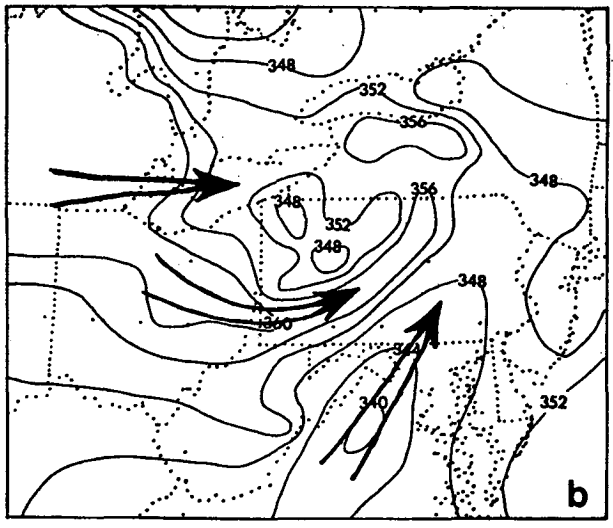

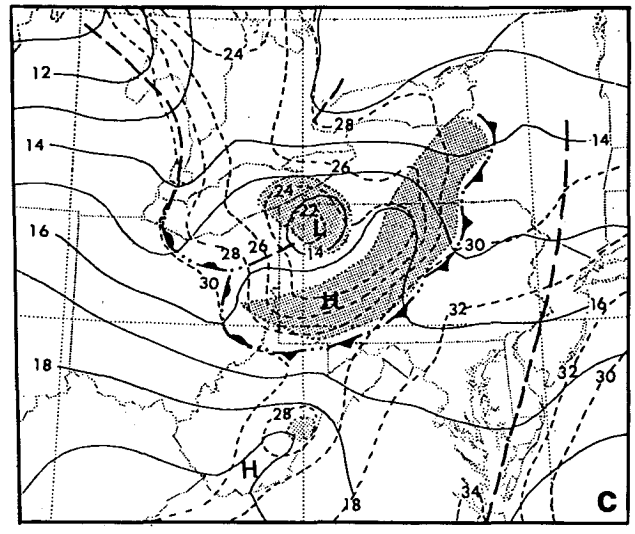

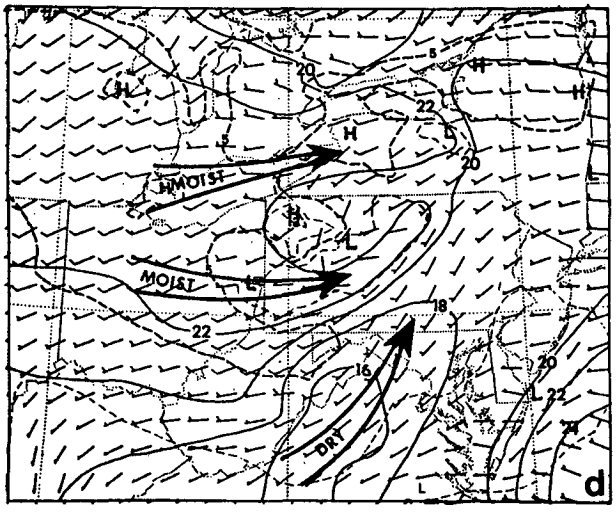

FIG. 13a. Mesoscale analysis for 1800 GMT 19 July 1977 (adapted from H78). Heavy dashed lines indicate troughs. Cold and warm-frontal symbols alternated with double dots indicate moist-downdraft outflow boundaries. The light shading denotes the level-1 radar echoes and the dark shading denotes level-3 (or greater) radar echoes. Reflectivity boundary is not defined if the echo contour is open. A full wind barb is 5 m s^{-1}.

FIG. 13b. Analysis of surface equivalent potential temperature (K) for 6 h forecast verifying at 1800 GMT 19 July 1977. Large arrows denote surface flow.

FIG. 13c. As in Fig. 12a but for 6 h forecast verifying at 1800 GMT 19 July 1977.

FIG. 13d. As in Fig. 11b but for 6 h forecast verifying at 1800 GMT 19 July 1977. Large arrows indicate the dry and moist tongues.

terly flow brought lower-θ_e air (i.e., cold and dry) into eastern Pennsylvania, thus tending to temporarily suppress the occurrence of convection and slow the propagation of the squall line into the eastern part of the state.

Significant changes in the wind field are also evident at 1800 GMT. Specifically, winds in the center of the cool pool associated with the squall line diminished substantially from speeds present in that region prior to convection. While this is not apparent in the 1800 GMT observations, it is a characteristic common to downdraft-produced mesohighs and is clearly evident in the 2100 GMT observations when the mesohigh became larger and stronger. It is also apparent from Fig. 13a that there are few observing stations near the ridge line where such light winds would be expected. Another feature evident in the model-predicted wind field is the high degree of horizontal shear and strong cross-isobaric motion. This is probably an indication of the large ageostrophic adjustments taking place in response to the forcing from the deep convection (see Perkey and Maddox, 1985). Finally, it is very important to note that the high wind speeds have *developed* around the meso-β low over northwestern Pennsylvania. These strong winds continue to increase until approximately 0000 GMT, after which they rapidly subside. While the model results show higher wind speeds near the mesolow, there are no reports of sustained surface winds of this magnitude in the observations. This may be a result of overprediction of the mesolow.

By 2100 GMT, the simulated squall line has moved into central Pennsylvania and is roughly parallel to the Appalachians (see Figs. 14b and c). Compared with observations (Fig. 14a), the northern end propagated a little too fast while the southern end propagated slightly too slow. This leads to the occurrence of convection over eastern West Virginia rather than western Virginia. Correspondingly, the pressure trough–ridge system at its southern point weakened as the area and strength of convection decreased. However, both the closed mesohigh and low associated with the squall line are well developed as observed in reality. While the squall line gradually moved into the lower-θ_e region (see Fig. 13b) and tended to dissipate thereafter, the MCC was intensifying. The pool of cool moist downdraft air associated with the MCC moved with the mesolow but lagged behind it. At this time, the circular-shaped MCC present three hours ago became elongated in a west–east direction, which is in excellent agreement with the radar and satellite observations. The relative positions of the various mesohighs and mesolows agree extremely well with the observed locations (compare Figs. 14a and 14b). However, it is apparent that, in general, the highs are too weak and the lows are too strong. This is particularly true for the mesohigh over south-central Pennsylvania and the closed mesolow over the north-central part of the state. Possible reasons for such systematic departures are discussed later.

In response to the strong afternoon surface heating and the low-level moisture advection, a warm and humid PBL formed west of the MCSs. Both surface reports and model forecasts confirm the development of this warm and humid layer. Moreover, satellite imagery during 1800–2100 GMT (see Fig. 10) shows many organized "cloud streets" aligned parallel to the mean wind within the PBL with a few isolated small areas of deep convection sporadically appearing and then dissipating. According to Brown (1980) and LeMone (1973, 1976), such "cloud streets" generally indicate an unstable stratification in the PBL. Apparently, the existence of this unstable air was indicative of the continued supply of high-θ_e air into the MCSs from late afternoon through nighttime hours (see θ_e distribution at 1800, 0000 and 0600 GMT). A new area of convection developed at this time to the west of the MCC but east of the trough that was present over Ohio three hours ago. Observations at 2000 GMT indicate that the actual convective events occurred two–four grid lengths east of the predicted locations (see Fig. 8c in H78). To the north of the MCC, the high pressure ridge over Ontario became weaker as the effect of the clouds on the surface radiation budget was removed at 2000 GMT (see section 2c); the temperature gradient across the Great Lakes was maintained.

At 0000 GMT (see Figs. 15a–d), both the predicted and observed squall lines apparently moved into less favorable environments (lower-θ_e) and dissipated. Along with the residual convection from the squall line, a weakening low and a quasi-stationary mesohigh were left behind. The mesohigh developed anticyclonic flow over northeastern Pennsylvania as the cold downdraft air spread out in the boundary layer. It is particularly noteworthy that the model forecast continued intensification and expansion of the MCC during the six-hour period when the solar insolation rapidly diminishes. Moreover, the predicted location and orientation of the MCC compare well with the observed.

On the other hand, the model failed to predict the generation and eastward propagation of the small storm system that was observed to cross through the Pittsburgh area during the period 2000 to 0000 GMT (see Fig. 8 in H78). Rather, a small system formed slightly farther west than the observed system, as mentioned before. Therefore, instead of this storm merging with the MCC near Johnstown during this time period, the model predicted a more southerly propagation of the convection to the west of Johnstown. Northeast of Johnstown, the model-forecast mesolow gradually became more comparable in size to the observed, although still too strong. The maximum "surface" wind ($\approx$15 m above the actual surface) near the center of the predicted mesolow continuously increased from 13 m s^{-1} at 1800 GMT, to 19 m s^{-1} at 2100 GMT and

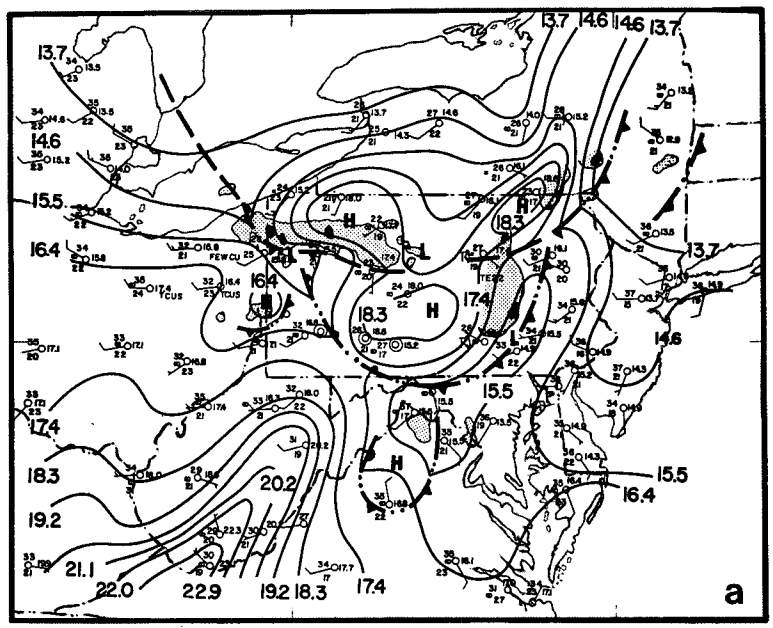

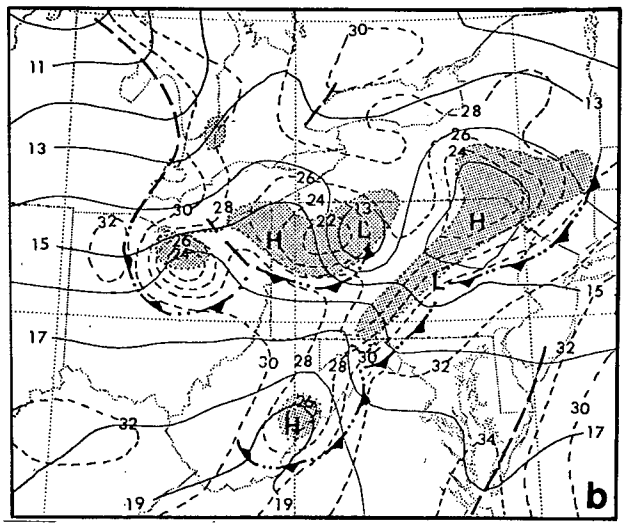

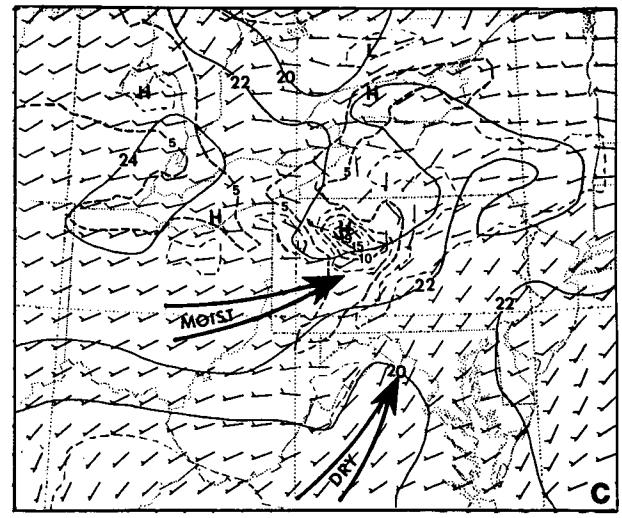

FIG. 14a. As in Fig. 13a but for 2100 GMT 19 July 1977.
FIG. 14b. As in Fig. 12a but for 9 h forecast verifying at 2100 GMT 19 July 1977.
FIG. 14c. As in Fig. 11b but for 9 h forecast verifying at 2100 GMT 19 July 1977. Large arrows indicate the dry and moist tongues.

to 21 m s^{-1} at this time, indicating continued intensification of the low. To the west of the mesolow, the observed mesohigh was well maintained by the model. To the west and north of the MCC the predicted attenuation of the pressure perturbations agrees well with H78's surface analysis. Comparisons of model-predicted temperature and dew points with observations are still favorable.

As the radar (Fig. 16a) and hourly rainfall analyses indicate (see Fig. 11 in H78), heavy precipitation fell at Johnstown and its adjacent region primarily during the period 0000–0600 GMT. The model convection continued to be active over a wide region just to the *west* of Johnstown during this period but did not propagate eastward (see Figs. 16a, b and 17a, c). Since the model-predicted conditions over Johnstown during this time were still conditionally unstable (not shown), the failure of the convection to develop over Johnstown is likely related to initial conditions, dynamical reasons, or the sensitivity of the procedure for initiating convection in the convective parameterization. Specifically, the initiation of deep convection over eastern Ohio and western Pennsylvania appeared to be sensitive to the degree of lifting resulting from the overrun-

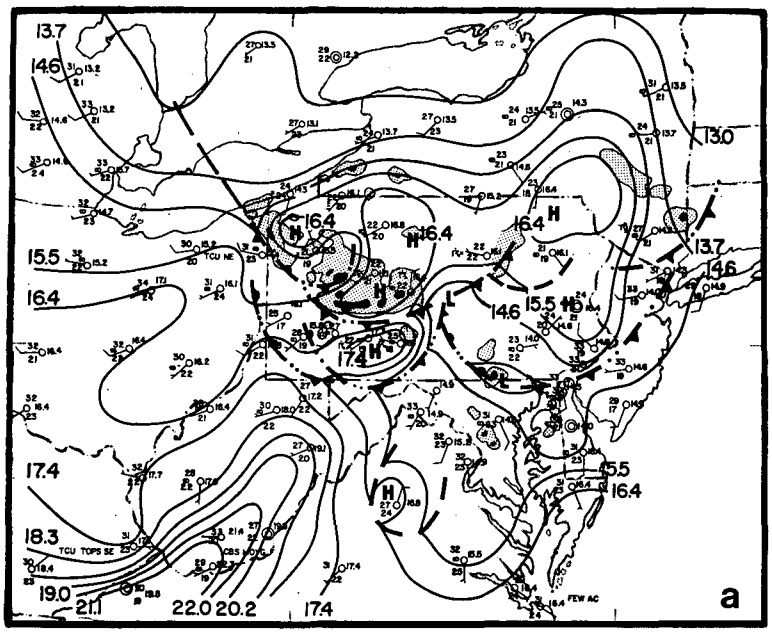

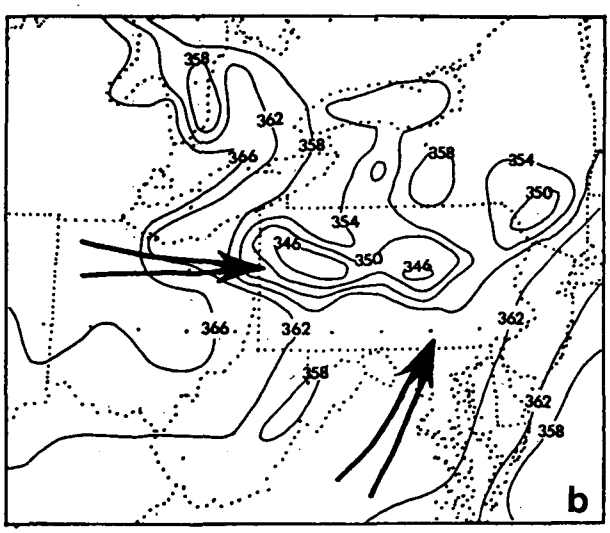

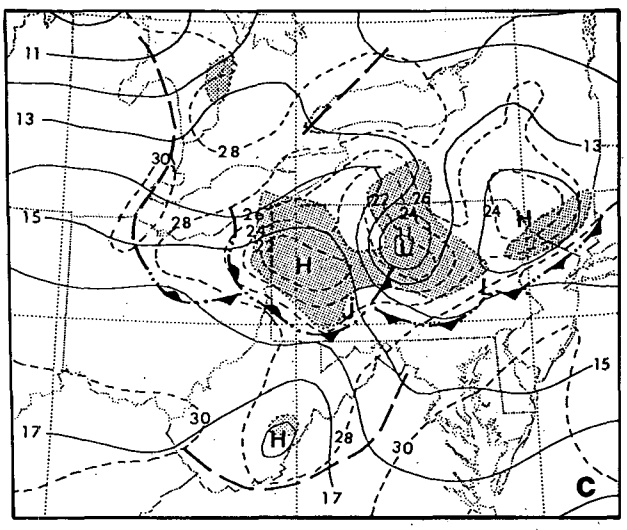

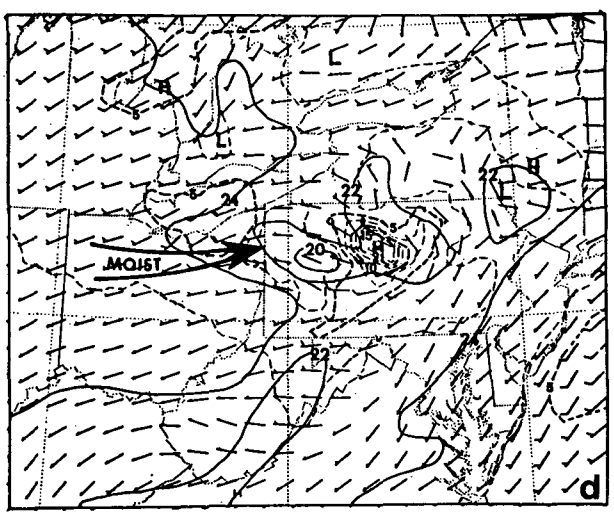

FIG. 15a. As in Fig. 13a but for 0000 GMT 20 July 1977.

FIG. 15b. As in Fig. 13b but for 12 h forecast verifying at 0000 GMT 20 July 1977.

FIG. 15c. As in Fig. 12a but for 12 h forecast verifying at 0000 GMT 20 July 1977.

FIG. 15d. As in Fig. 11b but for 12 h forecast verifying at 0000 GMT 20 July 1977.

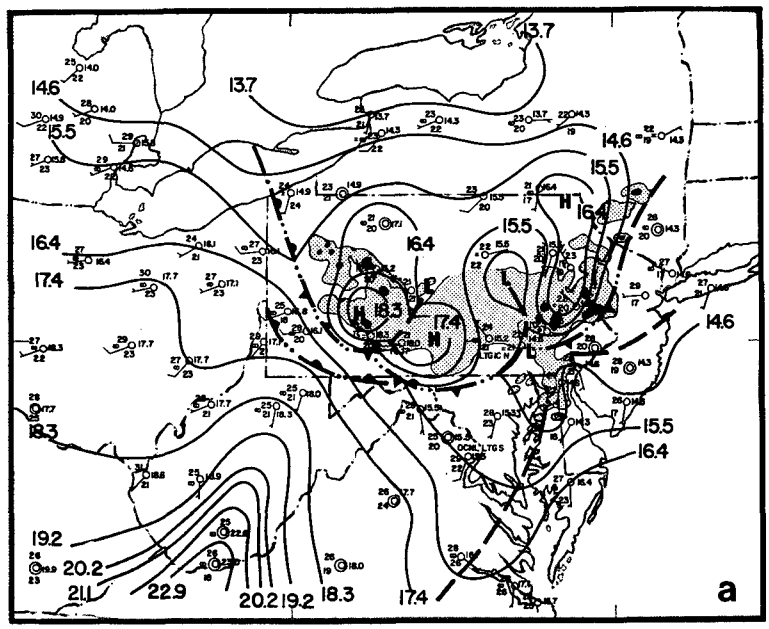

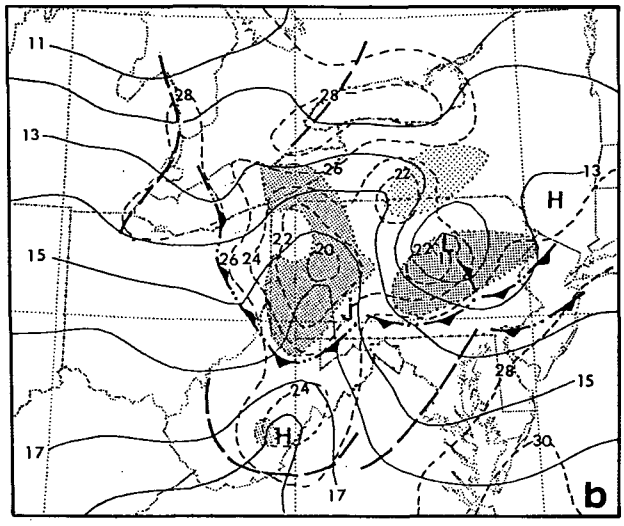

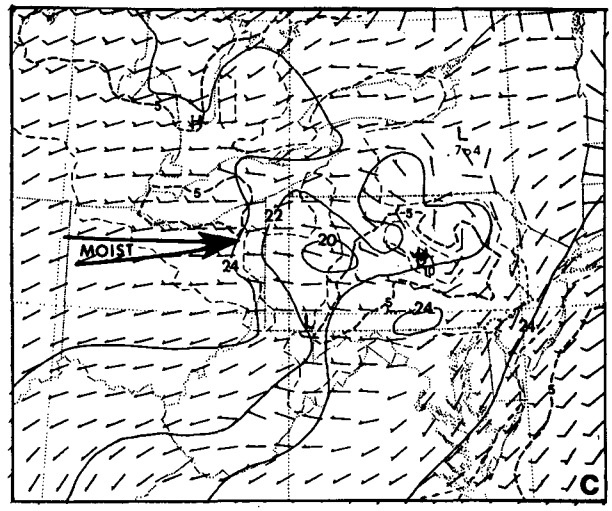

FIG. 16a. As in Fig. 13a but for 0300 GMT 20 July 1977.
FIG. 16b. As in Fig. 12a but for 15 h forecast verifying at 0300 GMT 20 July 1977. Lighter shading indicates shallow convection.
FIG. 16c. As in Fig. 11b but for 15 h forecast verifying at 0300 GMT 20 July 1977.

ning of cool downdraft air from previous convection. In particular, note that at 0000 GMT (Fig. 15b), high-θ_e air from Ohio was overrunning the layer of cool downdraft air produced by the thunderstorms that moved through the Pittsburgh area between 2100 and 0000 GMT. Yet, this lifting was insufficient to trigger very much new convection over extreme western and southwestern Pennsylvania. Significant areas of deep convection did not develop until the warm, moist boundry-layer air was forced to ascend over the deeper outflow layer farther east. This was clearly documented by H78. Of course, an additional consideration is that stronger "dynamic" forcing was occurring farther east and was instrumental in helping initiate the convection. This same scenario developed in the model, except slightly to the west of the observed events, i.e., a small area of convection and associated downdrafts were produced over Ohio but the primary area of deep convection remained farther east (see Figs. 14b, 15c and 16b). Since the regions of strong mesoscale ascent (dynamic forcing) and the outflow boundaries are very much determined by the convection itself (e.g., see

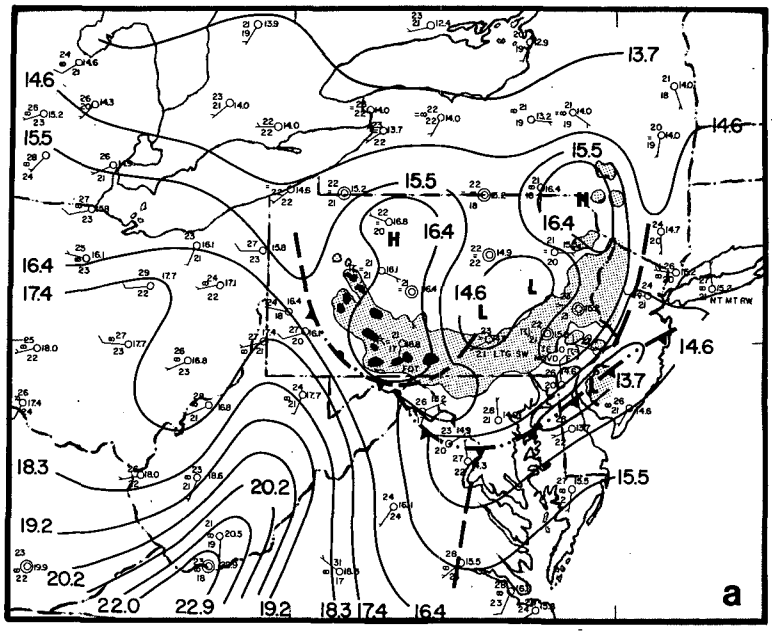

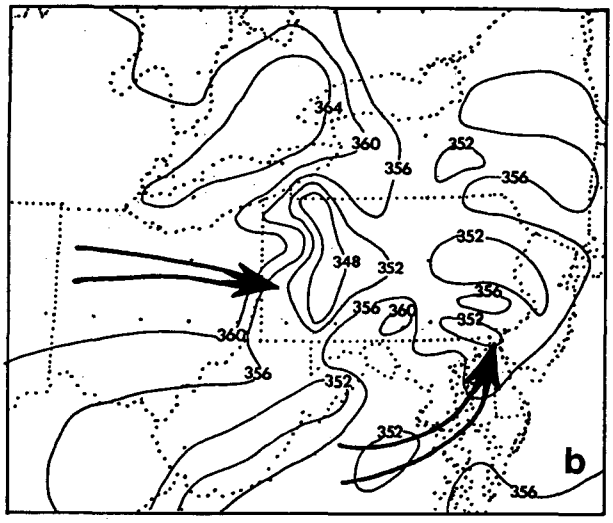

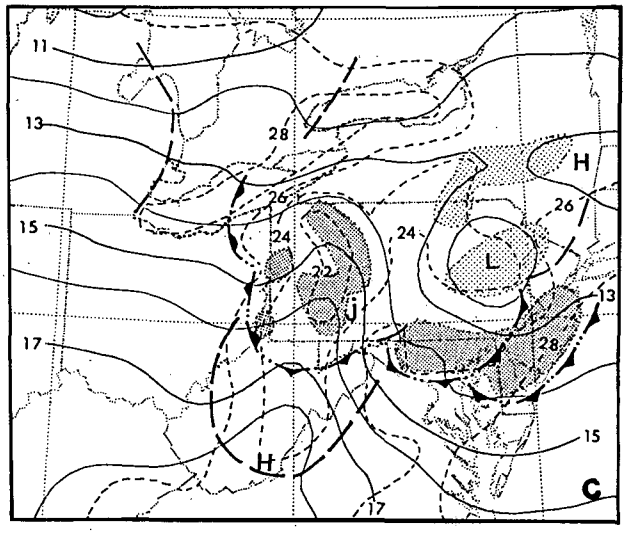

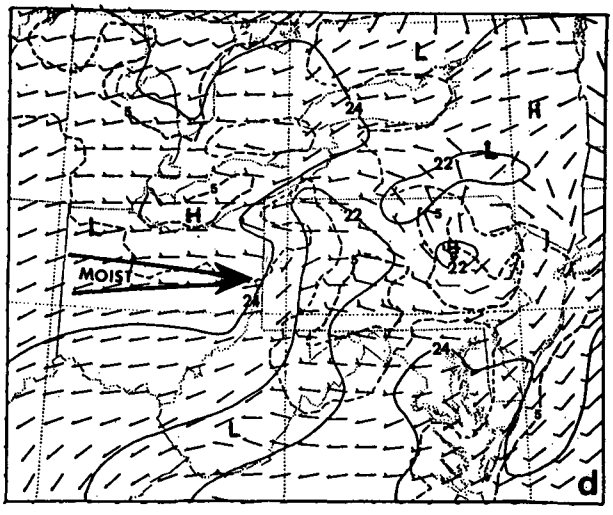

FIG. 17a. As in Fig. 13a but for 0600 GMT 20 July 1977.

FIG. 17b. As in Fig. 13b but for 18 h forecast verifying at 0600 GMT 20 July 1977.

FIG. 17c. As in Fig. 12a but for 18 h forecast verifying at 0600 GMT 20 July 1977. Lighter shading indicates shallow convection.

FIG. 17d. As in Fig. 11b but for 18 h forecast verifying at 0600 GMT 20 July 1977.

Fritsch and Chappell, 1980b; Fritsch and Maddox, 1981a), errors in the locations of previous deep convection can strongly impact the subsequent evolution of events.

At 0300 GMT, the deep convection comprising the model MCC was split into three parts: one each over eastern Pennsylvania, western Pennsylvania and south-central New York. While the radar summaries at 0300 GMT do not display a "cloud-free" region in the south-central part of Pennsylvania, this region exhibits only weak (level 1) radar returns with a diffuse (nondiscernable) boundary at the northern edge. The intense convection is clearly occurring in two distinct and separate zones over eastern and western Pennsylvania. Thus, the model is still exhibiting skill with respect to the time and space evolution of the mesoscale organization of the intense convection. On the other hand, the model erroneously predicted convection over south-central New York until 0600 GMT. Note, however, that the updrafts in this convection were marginally buoyant and cloud-top heights were substantially lower (by about 5–6 km) compared to the intense convection in the other two areas. This is also apparent in the 500 mb vertical motion field (Fig. 19), which shows very weak upward motions occurring over those regions with weak convection whereas stronger ascent is associated with the major MCS.

Near the end of the simulation, the model predicts that the outflow boundary over southeastern Pennsylvania will propagate through Maryland into Delaware and southern New Jersey and trigger a broad area of new convection (see Fig. 17c). While it is readily apparent from Figs. 17a and 18 that the cool thunderstorm-outflow air did indeed advance into this region, new convection there was observed to be widely scattered at this time. A sensitivity test with no parameterized moist downdrafts (see Zhang, 1985) shows no sign of propagation of convection into this region, confirming the important role of the cool outflow boundary in triggering this area of convection. Note, however, that by 0800 GMT (see Fig. 8 in H78), widespread convection had developed in this region as the convective complex slowly shifted southeastward. Possible reasons for the model-predicted convection developing too soon in this region were mentioned in the discussion of the failure of the model to predict deep convection over Johnstown. Considering that this is the 18th hour of a mesoscale simulation with very small grid elements, the radar-observed distribution and configuration of convection are fairly well reproduced. In particular, at this time the model simulated well most of the relative locations and strengths of the mesohighs and lows, and ridges and troughs. Also, as both the simulations and observations indicate, the two mesohighs north of the mesolow tended to merge at this time. In fact, H78's analysis (see Fig. 18) shows these two mesohighs as completely merged at 0700 GMT. Moreover, the nocturnal boundary layer for both the clear areas and cloudy regions is well reproduced. Finally, the high-θ_e air overrunning the cool outflow boundary is still evident, and this resulted in the continued model convection over western Pennsylvania.

b. Rainfall verifications

Precipitation is a very important end product of a model forecast. In this study, it is particularly important to ascertain whether or not fine-resolution mesoscale models can have a positive impact on the warm-season QPF. Figures 20 and 21 compare the model-predicted rainfall amounts with that from BS81's and H78's analyses. In general, the comparison of the magnitude and distribution of the precipitation is favorable. The model predicted the approximate *location* and *orientation* of the axes of maximum precipitation in northwestern and northeastern Pennsylvania. The difference in magnitude of the predicted maximum precipitation compared to BS81's observed at the northwestern corner of Pennsylvania is possibly due to the use of the relatively coarse network of hourly reporting stations. In fact, H78 (see Fig. 21a) used the much higher resolution 24 h (1200 GMT 19 July—1200 GMT 20 July) reporting network and their analysis shows a 100 mm rainfall maximum at the northwestern corner. Radar analyses from H78 clearly show that the bulk of the precipitation in this area fell during the first 12 h so that the model-predicted amounts are not unreasonable. The precipitation maximum over eastern West Virginia agrees with the location of convective storms visible in the satellite imagery (see Fig. 10) and with the radar observations. The BS81 analysis does not include the precipitation that fell along the eastern West Virginia border.

While an independent analysis of the observed accumulated rainfall distribution at 0600 GMT 20 July is not available, comparison of the observed 12 h rainfall amounts (Fig. 20a) to the 24 h amounts (Fig. 21a) clearly indicates a nocturnal maximum near Johnstown. Comparison of the 12 and 18 h forecast (Figs. 20b and 21b) shows a southerly propagation of heavy precipitation *to the west* of Johnstown (compare the 15 and 40 mm contour from Fig. 20b to 21b). This agrees with the nocturnal precipitation maximum reported in the vicinity of Johnstown. In the model, however, all precipitation *at* Johnstown seems to be a result of the squall line. Rainfalls over southeastern Pennsylvania, northern Virginia and Delaware are fairly reasonable if compared to BS81's analysis for the period 0000 GMT–1200 GMT 20 July.

It is very important to point out that grid-scale resolvable precipitation from mesoscale moist ascent within the MCSs made a significant contribution (30%–40%) to the total rainfall (see Zhang, 1985). This was

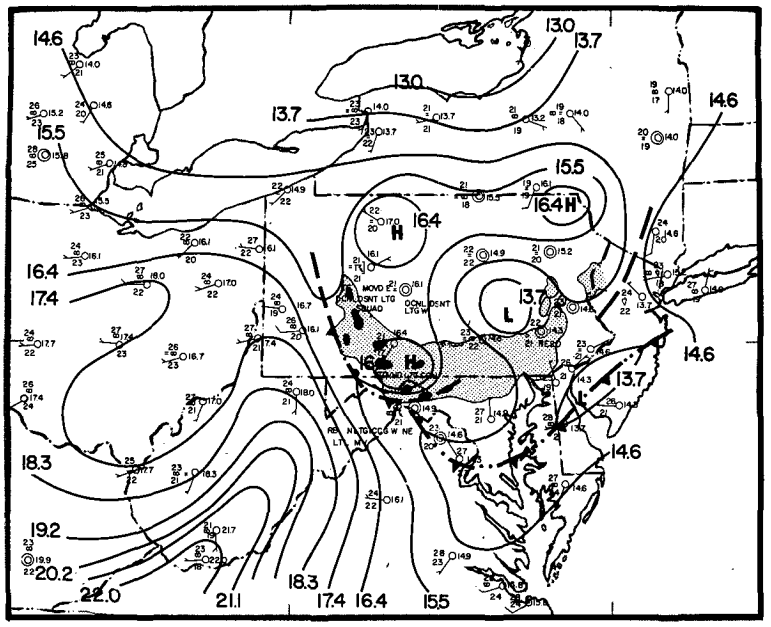

FIG. 18. As in Fig. 13a but for 0700 GMT 20 July 1977.

also true in the recent study of an MCC by Perkey and Maddox (1985) and in observational studies of tropical cloud clusters by Houze (1977). As shown by Zhang and Fritsch (1985), the axis of the heaviest rainfall correlates well to the path of the mesolow. It is also important to point out that the model was unable to produce the extremely heavy rainfall that occurred near Johnstown between 0000 GMT and 1200 GMT 20 July (compare Figs. 20a and 21a). Note, though, that in the period 0000 to 0600 GMT, the model predicted a lobe of heavy precipitation over southwestern Pennsylvania (compare Figs. 20b and 21b). The inability of the model to generate the very heavy rains near Johnstown is probably due to deficiencies in the model physics and/or initial conditions. Of course it should also be borne in mind that an 18 h forecast is near the theoretical limit imposed on meso-β scale predictability (see Anthes et al., 1985; Stull, 1985).

c. *Simulation of large-scale features*

For the present case, both H78 and BS81 pointed out that the meso-α scale short-wave trough accompanying the migrating MCSs played a key role in determining the structure and evolution of the flooding rain event. On the other hand, sensitivity tests (see Zhang, 1985) suggest that the evolution of the short-wave trough and a low-level jet is strongly related to the development of the MCSs. In order to show the performance of the nested-grid model in producing two-way interaction between the MCSs and larger-scale environment, the 12-h predicted upper air features from the CGM framework are compared to the independent subjective analysis by H78 and to objective analyses of some of the sounding data.

Figure 22 compares the model-simulated 850 mb features at 0000 GMT 20 July 1977 to H78's analyses and objective analyses of the observed winds. All objective analyses were done using the Cressman-type technique (Benjamin and Seaman, 1985). For the most part, the model captured the major features present in

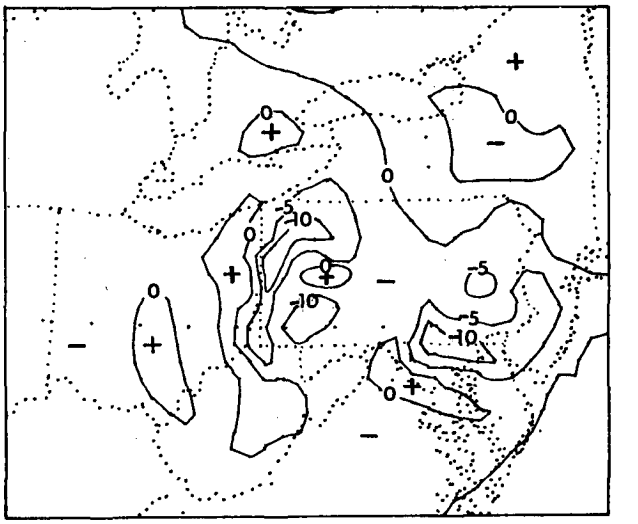

FIG. 19. Vertical motion (ω, μb s^{-1}) distribution at 500 mb for 18 h forecast verifying at 0600 GMT 20 July 1977.

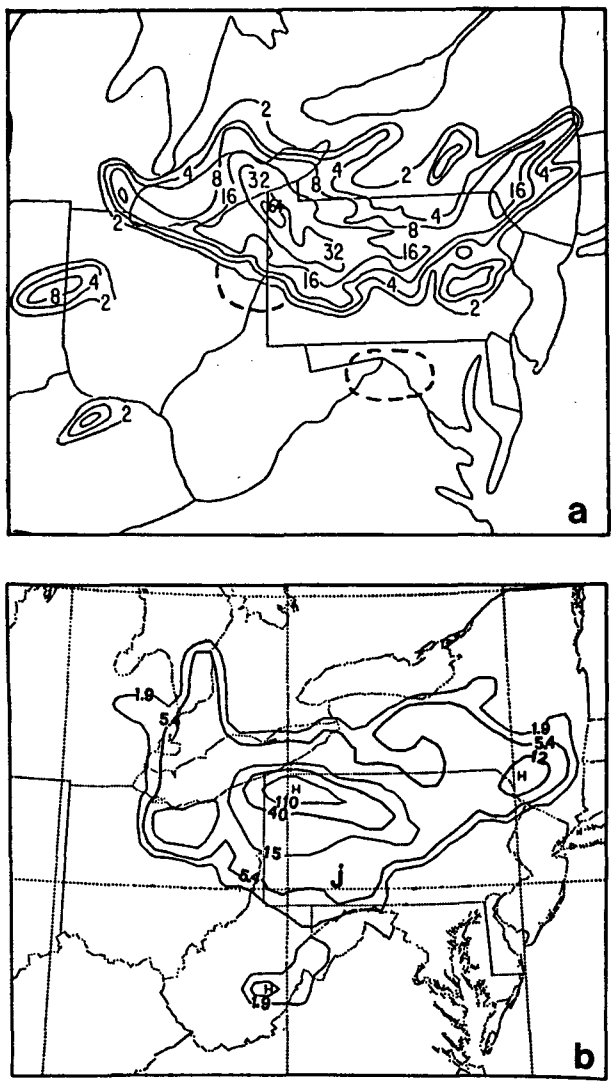

FIG. 20. Comparison of the observed (*a*, from BS81) accumulated rainfall (mm) with the predicted (b) for the period 1200 GMT 19 July 1977 to 0000 GMT 20 July 1977. The dashed line in (a) indicates the approximate location of precipitation observed by radar and satellite (see Figs. 14a and 15a).

the low-level wind field at 0000 GMT. In particular, the model predicted the narrow zone of the low-level jet over Pennsylvania, although the location of the speed maximum differed slightly from the observed. The difference in the maximum speed and the position of the 15 m s^{-1} isotach near the MCSs may be due to the fact that there was only one rawinsonde observation (Pittsburgh) within Pennsylvania at this time, while most of the convective activity occurred over regions east of Pittsburgh. Hence, the exact location of such detailed features cannot easily be resolved by the observational network. On the other hand, to the north of Pennsylvania, the weak wind zone picked up by the

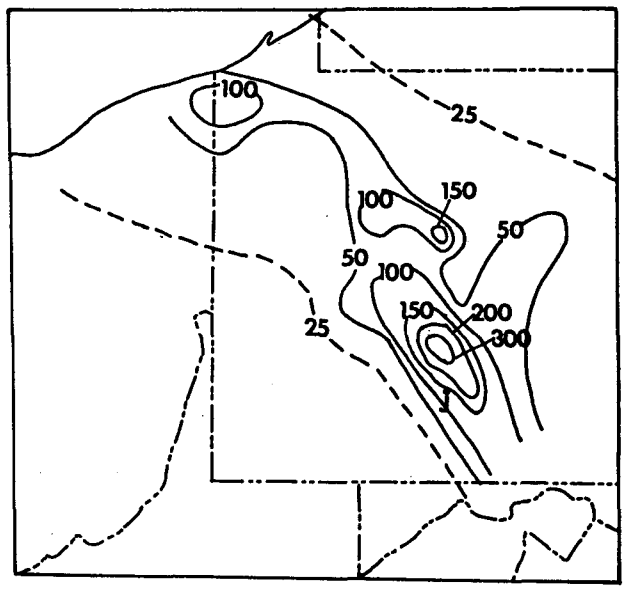

FIG. 21a. Observed 24 h accumulated rainfall (mm) from 1200 GMT 19 July 1977 to 1200 GMT 20 July 1977 (adapted from H78).

Buffalo and Albany, New York, soundings is well simulated by the model.

Comparisons of model-predicted to observed horizontal winds above 850 mb (700 mb, Figs. 23b and 23d; and 500 mb, Figs. 24b and 24d) are favorable in many general respects. For example, both observations and forecasts clearly show the strong versus weak wind contrast in the vicinity of the mesovortex. Over the northern portion of the domain, the strong horizontal and vertical wind shears associated with the large-scale

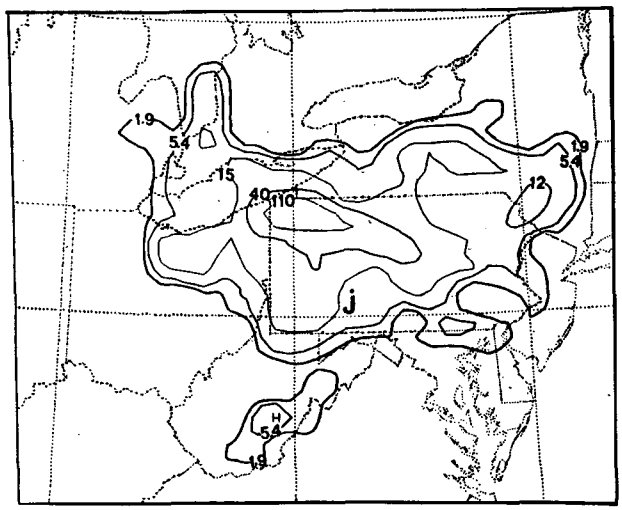

FIG. 21b. Predicted accumulated 18 h rainfall (mm) during 1200 GMT 19 July 1977 to 0600 GMT 20 July 1977.

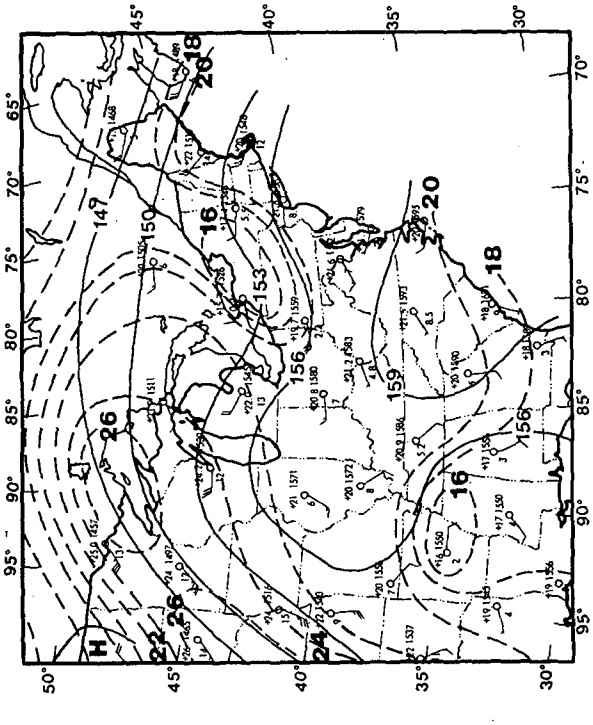

FIG. 22a. Analysis of 850 mb heights (thick solid lines, dam), temperature (thin solid lines, °C) and dewpoint for 0000 GMT 20 July 1977 (reproduced from H78). A full barb is 5 m s^{-1}.

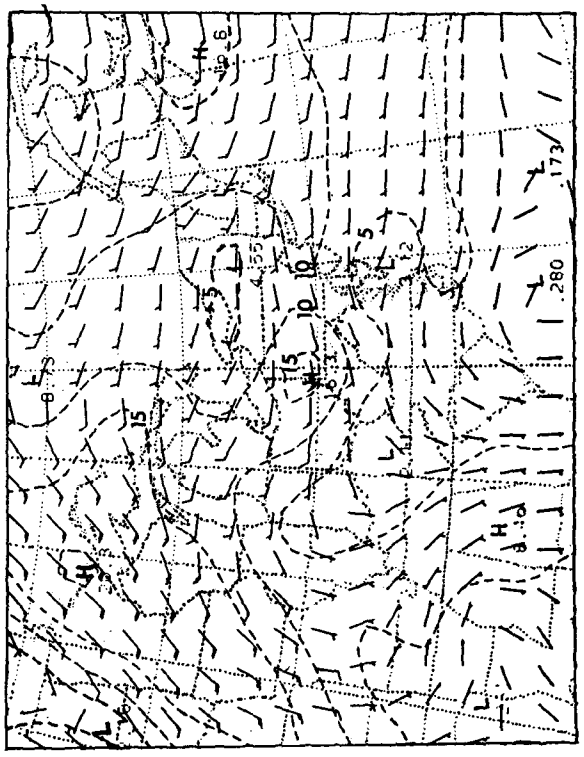

FIG. 22b. Analysis of 850 mb horizontal winds (m s^{-1}) for 0000 GMT 20 July 1977. A full barb is 10 m s^{-1}.

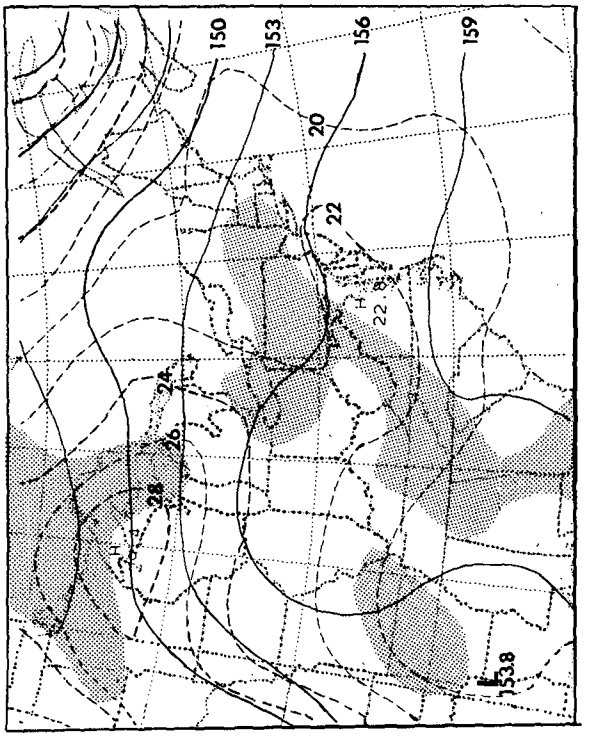

FIG. 22c. 12 h forecast of height (solid lines, dam), temperature (dashed lines, °C) and dewpoint ($T_d \geq 16$°C is shaded) for 850 mb, verifying at 0000 GMT 20 July.

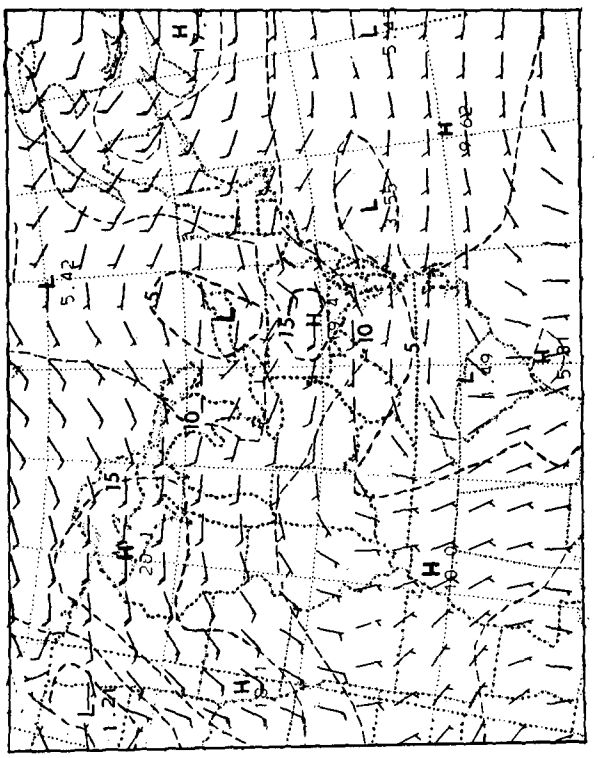

FIG. 22d. 12 h forecast of 850 mb horizontal winds (m s^{-1}), verifying at 0000 GMT 20 July. A full barb is 10 m s^{-1}.

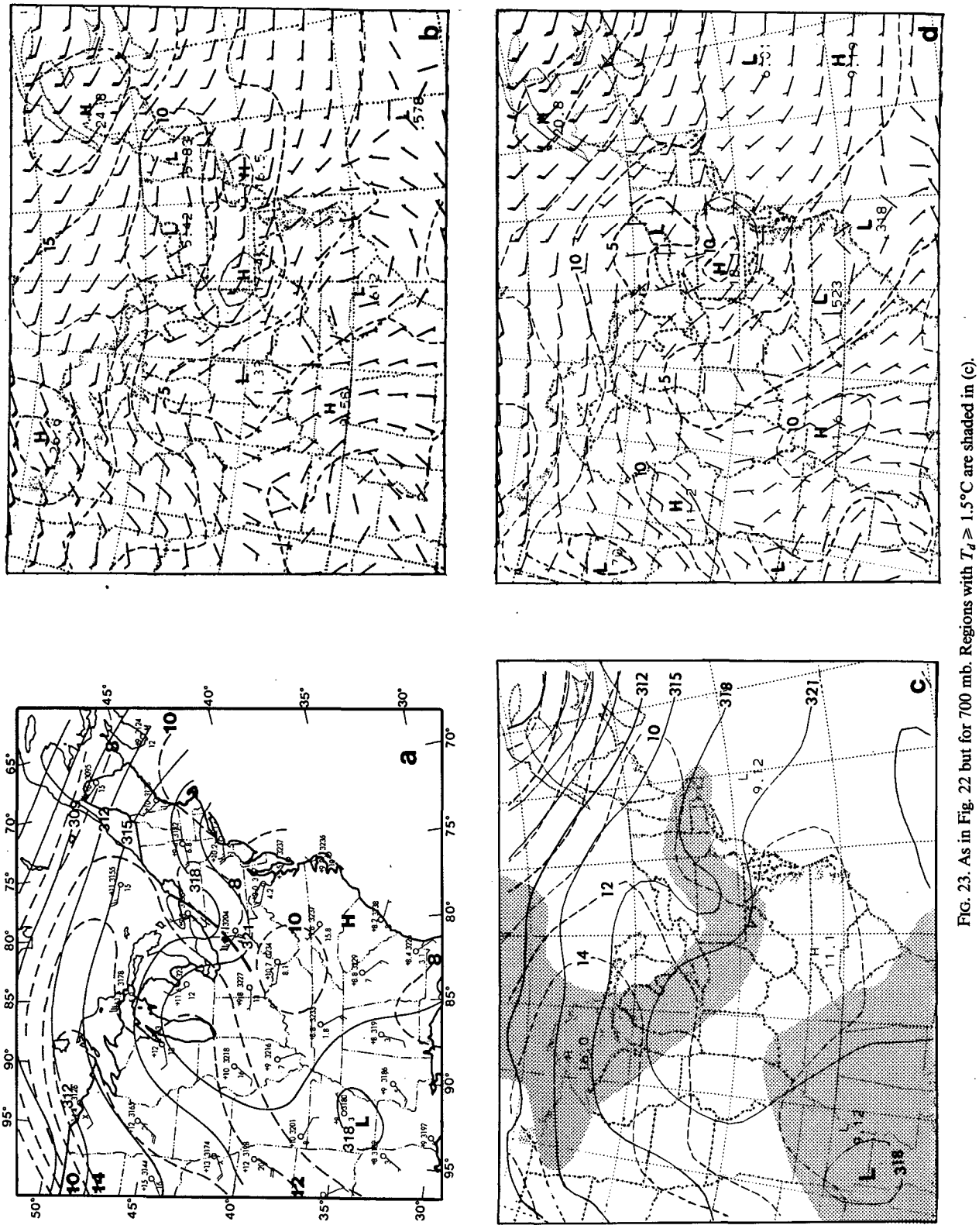

FIG. 23. As in Fig. 22 but for 700 mb. Regions with $T_d \geq 1.5$°C are shaded in (c).

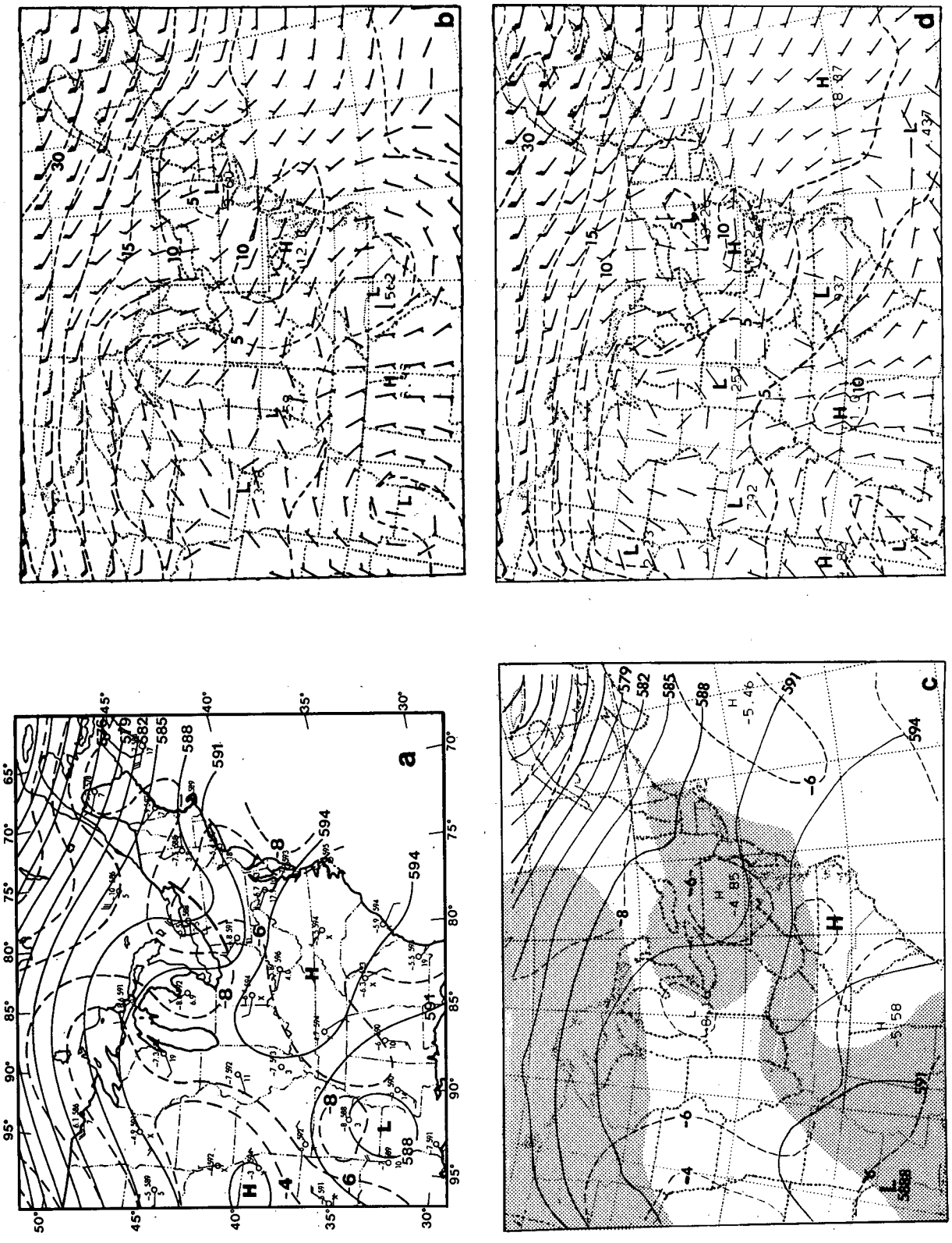

FIG. 24. As in Fig. 22 but for 500 mb. Regions with $T_d \geq -17$°C are shaded in (c).

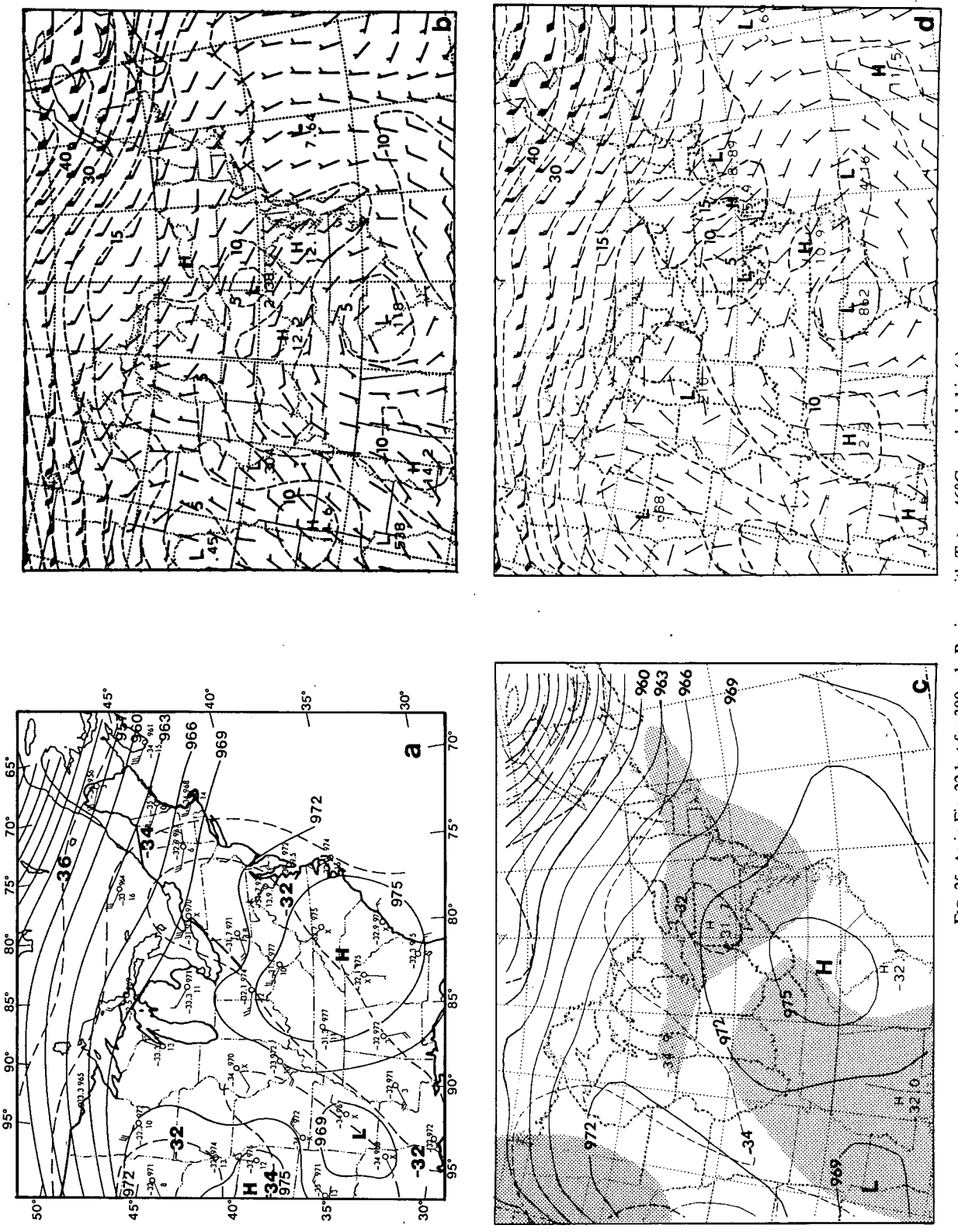

FIG. 25. As in Fig. 22 but for 300 mb. Regions with $T_d \geq -46°C$ are shaded in (c).

baroclinic zone in southeastern Canada are well reproduced. Near the CGM boundaries, the "one-way" nested approach of Perkey and Kreitzberg (1976) provided reasonable solutions in comparison with observations at all levels.

The axis of the short-wave trough, initially situated over Lake Huron and Lake Erie at 1200 GMT, moved over the eastern states by 0000 GMT. In general, the location and amplitude of the predicted short-wave perturbation fields conform to H78's analyses and to the objective analyses of the rawinsonde data. In particular, the relatively cool layer in the lower-tropospheric (up to $\approx$700 mb) portion of the trough and the relatively warm layer above are duplicated reasonably well. The model was also able to reproduce the observed amplification of the short wave below 500 mb (see Figs. 22, 23 and 27). However, above 500 mb, heights are a little too high (by 10 to 15 m) and the short-wave trough tends to lose its structure. Note that when constructing their 300 mb height analysis, H78 placed a trough axis just to the west of Pittsburgh (see Fig. 25a). From a synoptic-scale standpoint, the southwesterly wind at Pittsburgh supports such a position. However, close examination of the forecast and observed soundings at Pittsburgh indicates that the 300 mb level is in a transition layer where winds are backing from brisk northwesterly to light easterly at higher levels (see Fig. 28). This anomalous change in speed and in direction is due to the blocking effect of the MCSs (see Fritsch and Maddox, 1981a; Fritsch and Brown, 1982) and is not a reflection of the short-wave axis. Specifically, note that in the CGM forecast (Fig. 25d) the winds in the vicinity of Pittsburgh are light westerly while over eastern Pennsylvania a northwesterly jetlet has developed. In the FGM forecast, the blocking effect is even more apparent and the 300 mb winds over western Pennsylvania are clearly southwesterly (see Fig. 26).

While the high-level pressure heights and winds exhibit small errors near the western edge of the MCSs region, the thermodynamic fields (temperature and moisture) are, in general, predicted fairly well near the MCSs. This is true except for the lower troposphere (700 mb and below) over Ontario, Canada, and northwestern New York. Figure 28 compares observations and forecasts of the vertical thermal structure for Pittsburgh, Pennsylvania, and Buffalo, New York. The model reproduced exceedingly well the vertical profile of temperature and dewpoint for Pittsburgh. Both predicted and observed soundings show that the daytime mixed layer developed as high as 850 mb. The successful duplication of the vertical thermal and wind fields west of the MCSs are considered to be very important for showing the model's capability in generating the persistent convective activity over western Pennsylvania during evening hours. However, the model sounding for Buffalo indicates too much warming and drying below 650 mb in comparison with observation. This is most likely a consequence of overprediction of the mesolow as mentioned before (see Figs. 13c, 14b and 15c). Note that above 600 mb, the observed thermal structure is well simulated.

To the west of Pennsylvania, the temperature, moisture and height fields associated with the large-scale ridge are simulated fairly well. The same is true for the closed low in the southwest corner of the domain. The model-forecasted large-scale features at 0600 GMT July 20 also conform qualitatively to the H78 analysis for 1200 GMT July 20 (see Zhang, 1985).

5. Summary and concluding remarks

Modifications and improvements that help the PSU/NCAR numerical model simulate meso-β scale convectively generated features have been described. In particular, a two-way interactive nested-mesh system for the PSU/NCAR three-dimensional model has been adapted to include: (i) the Fritsch/Chappell convective scheme for the FGM; (ii) an Anthes/Kuo type convective scheme for the CGM; (iii) a PBL package for the nested meshes; (iv) one-way nesting type conditions for the CGM outermost boundary; and (v) virtual temperature effect.

The Johnstown flash flood of July 1977 was selected to test the model's ability to simulate meso-β scale features and heavy rain. Compared to the documentation of H78, the model reproduced fairly well many of the different atmospheric features of the Johnstown flood. In particular, the simulation was able to capture the size, orientation and propagation rate of the major meso-β scale convective features, i.e., the squall line and the MCC. Correspondingly, the model also reproduced the evolution of the surface pressure perturbations, such as meso-β scale lows, highs, ridges and

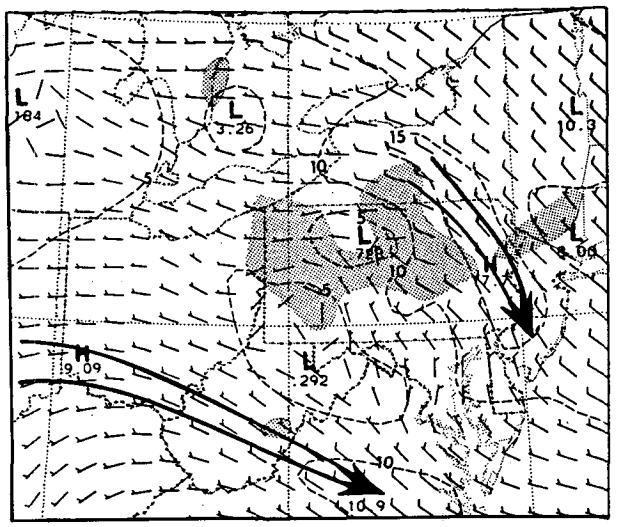

FIG. 26. 12 h forecast of the FGM horizontal winds (m s^{-1}) at 300 mb, verifying at 0000 GMT 20 July. A full barb is 10 m s^{-1}.

troughs. The magnitude and location of these features compared favorably to observations although the major mesolow is too strong and the mesohighs are a little too weak. Although the model failed in duplicating the continuous evening convection in the immediate vicinity of Johnstown, it did simulate the persistent nocturnal convective activity and the quasi-stationary outflow boundary slightly to the west of Johnstown. The model also simulated the diurnal cycle of the planetary boundary layer and the downdraft-generated temperature and dewpoint perturbations. Other mesoscale features, for example, low-level jets, meso-α scale short-wave and maximum/minimum horizontal wind couplets associated with the MCSs were also reproduced fairly well. Of particular significance is that the model-forecast rainfall amounts and distribution are similar to the observed.

Recognizing that a single case study does not provide a rigorous test of the predictability of a model, the results imply that it may be possible to forecast the meso-β scale structure and evolution of convective weather systems with useful skill for periods up to about 18 h. This agrees with the recent analyses of predictability by Stull (1985) and previous predictability concepts presented by Anthes (1984), Anthes and Baumhefner (1984) and Anthes et al. (1985). The results also imply that significant improvements in warm-season quantitative precipitation forecasts might be possible if numerical forecasts of the meso-β scale structure and evolution of convective weather systems became operational.

Acknowledgments. This work was supported by NSF Grants ATM-8218208 and ATM-8113223; USAF AFOSR-83-0064; and NOAA Cooperative Agreement NA82AA-H-00027. The authors are grateful to Lance Bosart and John Molinari for providing the dataset for the initial conditions, to Richard Anthes and William Cotton for their critical reviews, and to Michele Shawver for skillfully preparing the manuscript. The computations were performed at the National Center for Atmospheric Research, which is sponsored by the National Science Foundation.

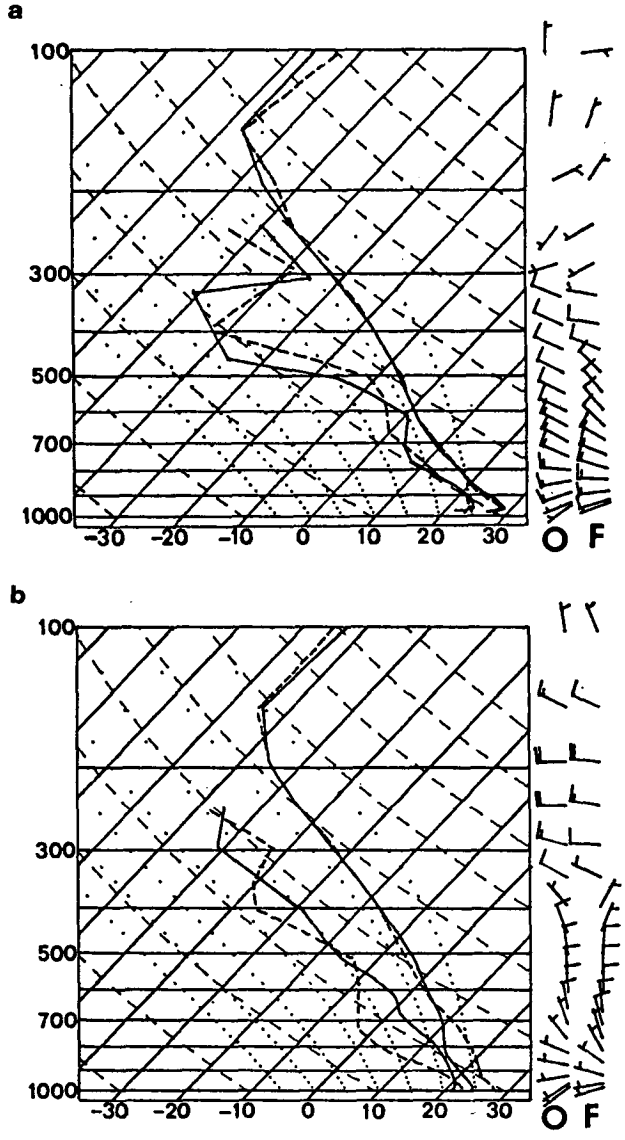

FIG. 28. Upper air sounding comparison of the observed (solid) with the predicted for 0000 GMT 20 July 1977. The letters "O" and "F" denote the observed and forecast winds, respectively. A full barb is 10 m s^{-1}. (a) Pittsburgh; (b) Buffalo.

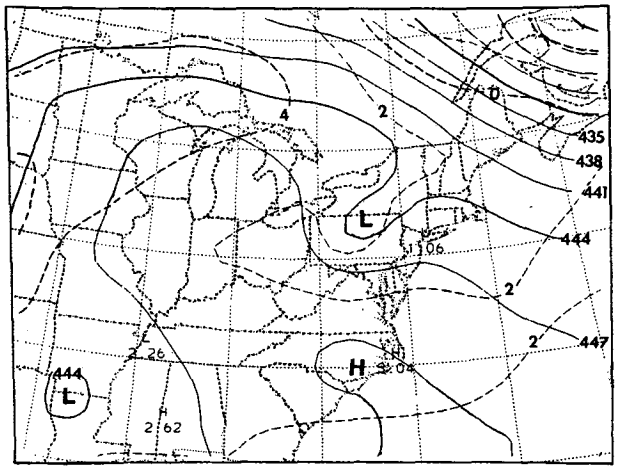

FIG. 27. As in Fig. 22c but for 600 mb and shading excluded.

REFERENCES

Anthes, R. A., 1977: A cumulus parameterization scheme utilizing a one-dimensional cloud model. *Mon. Wea. Rev.*, **105**, 270–286.

——, 1984: The general question of predictability. Lecture for AMS short course on mesoscale meteorology and forecasting. NCAR manuscript 0901-84-04, 38 pp.

——, and T. T. Warner, 1978: Development of hydrodynamic models suitable for air pollution and other mesometeorological studies. *Mon. Wea. Rev.*, **106**, 1045–1078.

——, and D. Keyser, 1979: Tests of a fine-mesh model over Europe and the United States. *Mon. Wea. Rev.*, **107**, 963–984.

——, and D. P. Baumhefner, 1984: A diagram depicting forecast skill and predictability. *Bull. Amer. Meteor. Soc.*, **65**, 701–703.

——, E.-Y. Hsie, D. Keyser and Y.-H. Kuo, 1981: Impact of data and initialization procedures on variations of vertical motion and precipitation in mesoscale models. *Preprints IAMAP Third Scientific Assembly*, Hamburg, IAMAP, 245–257.

——, Y.-H. Kuo, D. P. Baumhefner, R. M. Errico and T. M. Bettge, 1985: Predictability of mesoscale atmospheric motions. *Advances in Geophysics*, Vol. 28, Academic Press, 159–202.

Asselin, R., 1972: Frequency filter for time integration. *Mon. Wea. Rev.*, **100**, 487–490.

Barnes, S. L., 1974: Mesonetwork array, its effect on thunderstorm flow resolution. NOAA Tech. Rep. ERL NSSL-74, 16 pp.

Bean, B. R., R. Gilmer, R. L. Grossman and R. McGavin, 1972: An analysis of airborne measurements of vertical water vapor flux during BOMEX. *J. Atmos. Sci.*, **29**, 860–869.

Benjamin, S. G., 1983: Some effects of heating and topography on the regional severe storm environment. Ph.D. thesis, The Pennsylvania State University, 265 pp.

——, and N. L. Seaman, 1985: A simple scheme for improved objective analysis in curved flow. *Mon. Wea. Rev.*, **113**, 1184–1198.

Blackadar, A. K., 1978: Modeling pollutant transfer during daytime convection. *Preprints Fourth Symp. on Atmospheric Turbulence, Diffusion and Air Quality*, Reno, Amer. Meteor. Soc., 443–447.

Bosart, L. R., and F. Sanders, 1981: The Johnstown flood of July 1977: A long-lived convective storm. *J. Atmos. Sci.*, **38**, 1616–1642.

Braham, R. R., Jr., 1952: The water and energy budgets of the thunderstorm and their relation to thunderstorm development. *J. Meteor.*, **9**, 227–242.

Brown, H. A., and K. A. Campana, 1978: An economical time-differencing system for numerical weather prediction. *Mon. Wea. Rev.*, **106**, 1025–1036.

Brown, R. A., 1980: Longitudinal instabilities and secondary flows in the planetary boundary layer: A review. *Rev. Geophys. Space Phys.*, **18**, 683–697.

Caracena, F., and J. M. Fritsch, 1983: Focusing mechanisms in the Texas Hill Country flash floods of 1978. *Mon. Wea. Rev.*, **111**, 2319–2332.

——, R. A. Maddox, L. R. Hoxit and C. F. Chappell, 1979: Mesoanalysis of the Big Thompson storm. *Mon. Wea. Rev.*, **107**, 1–17.

Carlson, T. N., and F. E. Boland, 1978: Analysis of urban–rural canopy using a surface heat flux/temperature model. *J. Appl. Meteor.*, **17**, 998–1013.

Chang, C. B., D. J. Perkey and C. W. Kreitzberg, 1984: Impact of initial wind field on the forecast of a severe storm environment. *Preprints Tenth Conf. on Weather Forecasting and Analysis*, Clearwater, Amer. Meteor. Soc., 513–520.

Charba, J. P., and W. H. Klein, 1980: Skill in precipitation forecasting in the national weather service. *Bull. Amer. Meteor. Soc.*, **61**, 1546–1555.

Chen, C., and H. D. Orville, 1980: Effects of mesoscale convergence on cloud convection. *J. Appl. Meteor.*, **19**, 256–274.

Delsol, F., K. Miyakoda and R. H. Clarke, 1971: Parameterized processes in the surface boundary layer of an atmospheric circulation model. *Quart. J. Roy. Meteor. Soc.*, **97**, 181–208.

Eom, J., 1975: Analysis of the internal gravity wave occurrence of April 19, 1970 in the Midwest. *Mon. Wea. Rev.*, **103**, 217–226.

Estoque, M. A., 1968: Vertical mixing due to penetrative convection. *J. Atmos. Sci.*, **25**, 1046–1051.

Fritsch, J. M., 1975: Cumulus dynamics: Local compensating subsidence and its implications for cumulus parameterization. *Pure Appl. Geophys.*, **113**, 851–867.

——, and C. R. Chappell, 1980a: Numerical prediction of convectively-driven mesoscale pressure systems. Part I: Convective parameterization. *J. Atmos. Sci.*, **37**, 1722–1733.

——, 1980b: Numerical prediction of convectively-driven mesoscale pressure systems. Part II: Mesoscale model. *J. Atmos. Sci.*, **37**, 1734–1762.

——, and R. A. Maddox, 1981a: Convectively-driven mesoscale pressure systems aloft. Part I: Observations. *J. Appl. Meteor.*, **20**, 9–19.

——, and ——, 1981b: Convectively-driven mesoscale pressure systems aloft. Part II: Numerical simulations. *J. Appl. Meteor.*, **20**, 20–26.

——, and J. M. Brown, 1982: On the generation of convectively-driven mesohighs aloft. *Mon. Wea. Rev.*, **110**, 1554–1563.

——, E. L. Magaziner and C. F. Chappell, 1980: Analytical initialization for three-dimensional numerical models. *J. Appl. Meteor.*, **19**, 809–818.

Fujita, T., 1959: Precipitation and cold-air production in mesoscale thunderstorm system. *J. Meteor.*, **16**, 454–466.

Georgakakos, K. P., and M. D. Hudlow, 1984: Quantitative precipitation forecast techniques for use in hydrologic forecasting. *Bull. Amer. Meteor. Soc.*, **65**, 1186–1200.

Hoxit, L. R., R. A. Maddox, C. F. Chappell, F. L. Zuckerberg, H. M. Mogil, I. Jones, D. R. Greene, R. E. Saffle and R. A. Scofield, 1978: Meteorological analysis of the Johnstown, Pennsylvania flash flood, 19–20 July 1977. NOAA Tech. Rep. ERL 401-APCL43, 71 pp.

Houze, R. A., Jr., 1977: Structure and dynamics of a tropical squall-line system. *Mon. Wea. Rev.*, **105**, 1540–1567.

Kane, R. J., Jr., C. R. Chelius and J. M. Fritsch, 1986: The precipitation characteristics of mesoscale convective weather systems, *J. Climate Appl. Meteor.*, (in press).

Kelly, G. A. M., G. A. Mills and W. L. Smith, 1978: Impact of Nimbus-6 temperature soundings on Australian region forecasts. *Bull. Amer. Meteor. Soc.*, **59**, 393–405.

Kondratzev, K. Y., 1969: *Radiation in the Atmosphere. Int. Geophys. Ser.*, Vol. 12, Academic Press, 912 pp.

Kuo, H. L., 1965: On the formation and intensification of tropical cyclones through latent heat release by cumulus convection. *J. Atmos. Sci.*, **22**, 40–63.

——, 1974: Further studies of the parameterization of the influence of cumulus convection on large-scale flow. *J. Atmos. Sci.*, **31**, 1232–1240.

LeMone, M., 1973: The structure and dynamics of horizontal roll vortices in the PBL. *J. Atmos. Sci.*, **30**, 1077–1091.

——, 1976: Modulation of turbulence energy by longitudinal rolls in an unstable boundary layer. *J. Atmos. Sci.*, **33**, 1308–1320.

Lenschow, D. H., 1970: Airplane measurements of planetary boundary layer structure. *J. Appl. Meteor.*, **10**, 874–884.

Lilly, D. K., 1960: On the theory of disturbances in a conditionally unstable atmosphere. *Mon. Wea. Rev.*, **88**, 1–17.

Lipps, F. B., and R. S. Hemler, 1985: Another look at the scale analysis for deep convection. *J. Atmos. Sci.*, **42**, 1960–1964.

McAnelly, R. L., and W. R. Cotton, 1981: The meso-β scale structure and precipitation characteristics of middle-latitude mesoscale convective complexes. *Preprints Fourth Conf. on Hydrometeorology*, Reno, Amer. Meteor. Soc., 81–87.

McCumber, M. C., and R. A. Pielke, 1981: Simulation of the effects of surface fluxes of heat and moisture in a mesoscale numerical model. 1. Soil layer. *J. Geophys. Res.*, **86**, 9929–9938.

McNider, R. T., and R. A. Pielke, 1981: Diurnal boundary-layer development over sloping terrain. *J. Atmos. Sci.*, **38**, 2198–2212.

Maddox, R. A., 1980: Mesoscale convective complexes. *Bull. Amer. Meteor. Soc.*, **61**, 1374–1387.

——, C. F. Chappell and L. R. Hoxit, 1979: Synoptic and meso-α scale aspects of flash flood events. *Bull. Amer. Meteor. Soc.*, **60**, 115–123.

Matthews, D. A., 1981: Observations of a cloud arc triggered by thunderstorm outflow. *Mon. Wea. Rev.*, **109**, 2140–2157.

Molinari, J., and T. Corsetti, 1985: Incorporation of cloud-scale and

mesoscale downdrafts into a cumulus parameterization: Results of one- and three-dimensional integrations. *Mon. Wea. Rev.*, **113,** 485–501.

Moncrieff, M. W., and J. S. A. Green, 1972: The propagation and transfer properties of steady convective overturning in shear. *Quart. J. Roy. Meteor. Soc.*, **98,** 336–352.

Perkey, D. J., 1976: A description and preliminary results from a fine-mesh model for forecasting quantitative precipitation. *Mon. Wea. Rev.*, **104,** 1513–1526.

——, and C. W. Kreitzberg, 1976: A time-dependent lateral boundary scheme for limited-area primitive equation models. *Mon. Wea. Rev.*, **104,** 744–755.

——, and R. A. Maddox, 1985: A numerical investigation of a mesoscale convective system. *Mon. Wea. Rev.*, **113,** 553–566.

Ramage, C. S., 1982: Have precipitation forecasts improved? *Bull. Amer. Meteor. Soc.*, **63,** 739–743.

Sellers, W. D., 1965: *Physical Climatology.* University of Chicago Press, 272 pp.

Shir, C. C., and R. D. Bornstein, 1977: Eddy exchange coefficients in numerical models of the planetary boundary layer. *Bound.-Layer Meteor.*, **11,** 171–185.

Smull, B. F., and R. A. Houze, Jr., 1985: A midlatitude squall line with a trailing region of stratiform rain: Radar and satellite observations. *Mon. Wea. Rev.*, **113,** 117–133.

Stull, R. B., 1985: Predictability and scales of motion. *Bull. Amer. Meteor. Soc.*, **66,** 432–436.

UCAR, 1983: *The National STORM Program—Scientific and Technological Bases and Major Objectives.* R. A. Anthes, Ed., 520 pp.

Uccellini, L. W., 1975: A case study of apparent gravity wave initiation of severe convective storms. *Mon. Wea. Rev.*, **103,** 497–513.

Ward, J. D., 1981: Spatial and temporal heavy rainfall patterns over land associated with weakening tropical cyclones. *Preprints Fourth Conf. on Hydrometeorology,* Reno, Amer. Meteor. Soc., 174–180.

Washington, W. M., and D. P. Baumhefner, 1975: A method of removing Lamb waves from initial data for primitive equation models. *J. Appl. Meteor.*, **14,** 114–119.

Weaver, J. F., and S. P. Nelson, 1982: Multiscale aspects of thunderstorm gust fronts and their effects on subsequent storm development. *Mon. Wea. Rev.*, **110,** 707–718.

Weisman, M. L., and J. B. Klemp, 1982: The dependence of numerically simulated convective storms on vertical wind shear and buoyancy. *Mon. Wea. Rev.*, **110,** 504–520.

Westphal, D. L., 1981: The interaction between radiative and boundary layer processes in stratus clouds. M.S. thesis, The Pennsylvania State University, 138 pp.

Zhang, D.-L., 1985: Nested-Grid Simulation of the Meso-β Scale Structure and evolution of the Johnstown Flood of July 1977. Ph.D. thesis, The Pennsylvania State University, 270 pp.

——, and R. A. Anthes, 1982: A high-resolution model of the planetary boundary layer—sensitivity tests and comparisons with SESAME-79 data. *J. Appl. Meteor.*, **21,** 1594–1609.

——, and J. M. Fritsch, 1985: Numerical simulation of a meso-β scale warm-core vortex over land. *Preprints 14th Conf. on Severe Local Storms.*, Amer. Meteor. Soc., J29-32.

——, H.-R. Chang, N. L. Seaman, T. T. Warner and J. M. Fritsch, 1986: A two-way interactive nesting procedure with variable terrain resolution. *Mon. Wea. Rev.*, **114,** 1130–1339.